Fold-related deformation bands in a weakly buried sandstone reservoir analogue: a multi-disciplinary case study from the Numidian (Miocene) of Sicily (Italy)

Gambino S. [1], Fazio E. [1,*], Maniscalco R. [1], Punturo R. [1], Lanzafame G.[2], Barreca G. [1], Butler R.W.H.[3]

[1]Università di Catania - Dpt. Biol. Geol. Envir. Sciences - Earth Sciences Section - Corso Italia 57 - 95127 Catania (Italy)

[2] Elettra- Sincrotrone Trieste, Syrmep beamline Department Strada Statale 14 - km 163,5 in AREA Science Park 34149 Basovizza, Trieste, Italy

[3] Geology and Petroleum Geology, School of Geosciences, University of Aberdeen, Aberdeen (UK)

* Corresponding author: Email: efazio@unict.it

Abstract

Deformation bands, usually recognised in association with faults, are here analyzed in relation to a tight syncline fold developed in the Miocene Numidian turbidites of Sicily. Deposited above a growing thrust-wedge and then buckled during continued deformation, their porous sandstones form subsurface gas reservoirs elsewhere in the system and are analogues for deepwater systems in general. Structural data have been collected and statistically analyzed to characterise preferred orientations and size parameters (thickness, spacing, length) of deformation bands. Two distinct populations relate to folding: the most recent one is NE-SW oriented, which produced the most prominent structures, whereas an older one is partially obliterated. Microscopic investigation reveals porosity decreases within deformation bands with respect to host rock. The principal deformation mechanisms are grain rotation/sliding and pore-collapse, consistent with folding having occurred under low burial conditions. Within the thrust wedge, near-surface folding is widespread, as indicated by growth strata. Thus we expect early-burial deformation bands of the types (compaction an shear bands) illustrated here to be a component of reservoir damage in subsurface examples.

Key words: *deformation bands; Numidian sandstones; porosity; X-ray microtomography; reservoir analogue*

1. Introduction

Arrays of deformation bands are one of the main structures (together with joints, veins and shear fractures) that accommodate distributed deformation in porous sandstones (Fossen et al., 2007; 2017). Most outcrop studies have focused on their distributions and attributes associated with damage zones adjacent to faults (e.g. Saillet and Wibberley, 2013; Rotevatn and Fossen, 2011; Farrell et al., 2014 and dozens more). However, a small number of studies examine the relationship between deformation bands and folding (e.g. Jamison and Stearns, 1982; Świerczewska and Tokarski, 1998). Here we examine deformation band formation associated with a fold in growth strata that were deposited above an evolving thrust wedge. The setting provides insight on the development of deformation bands during folding under low burial conditions.

The early-middle Miocene Numidian sandstone is part of a turbidite sequence that represents the earliest influx of quartz sand onto the juvenile thrust systems of Sicily and the southern Apennines of Italy (e.g. Thomas et al., 2010). It is characterized by thick, amalgamated sandstone beds, up to 50 m thick. In the subsurface these strata host important gas reserves that have been exploited since the 1960s (Gagliano, Sicily, Pieri and Mattavelli, 1986) and further exploration continues. These types of successions are important exploration targets in other compressional settings, especially those on deepwater continental margins. Understanding sand continuity and heterogeneity is important for evaluating economic potential and so substantial efforts have been directed at developing outcrop analogues for stratigraphic architecture. Likewise, there has been significant work on understanding the patterns of deformation associated with faults. However, there are very few studies on the character of distributed deformation associated with folding, especially under low burial conditions. These structures are likely to be incorporated during subsequent burial, for example into sub-thrust settings, and therefore could impact on reservoir performance. Our aim here is to provide such a study. Here we present a detailed petrographic and structural study of Numidian sandstones, cropping out near the village of Sperlinga (Enna province, Italy).

Deformation bands are common structures developed within porous rocks (Aydin and Johnson, 1978; Schultz and Siddharthan, 2005; Fossen et al., 2007). Their formation, as opposed to simple fractures and joints, depends on a number of factors including porosity, depth of burial and deformation rate. The development of deformation bands may change the petrophysical properties on a rock body (especially important for hydrocarbon reservoir performance), such as porosity variation (pore-space collapse), permeability variation (fluid-barriers formation), increasing compaction and rock-strength (strain hardening behaviour).

There are two main classifications for deformation bands - one based on kinematics (Aydin et al., 2006), and another on deformation mechanism (Fossen et al., 2007). Kinematic nomenclatures distinguish dilation, shear, and compaction bands (and hybrids between the three). The mechanistic nomenclature identifies four deformation mechanisms: granular flow (grain boundary sliding and grain rotation), phyllosilicate smearing, cataclasis (grain fracturing and grinding or abrasion), dissolution and cementation. These, in turn, are represented by four distinctive types of deformation band: disaggregation, cataclastic, phyllosilicate, and solution/cementation bands. The formation of specific types depends on, among other factors, depth of burial and phyllosilicate content (e.g. Fossen et al., 2007).

In this paper we will use the classification by Aydin et al., (2006) to characterise the main kinds of deformation bands occurring in the study area. In discussion, we adopt the classification by Fossen et al. (2007), because it allows us to develop interpretations of the genetic processes.

2. Geological setting

The Numidian sandstone is a hyper-mature quartz arenite derived from the African craton (e.g. Wezel, 1970; Johansson et al., 1998; Thomas et al., 2010) and deposited within the broad foredeep and frontal structures of the Apennine-Maghrebian thrust belt of the central Mediterranean. The thrust system is preserved in Sicily and Apennines of mainland Italy (Fig. 1a). It was active through the Tertiary with the modern thrust front lying in the Gela foredeep, offshore Sicily (e.g. Elter et al., 2003) and in the Bradanic trough. The system experienced rotational emplacement onto the adjacent foreland

(Speranza et al., 2003), respectively represented by the Hyblean plateau (Sicily) and Apulian peninsula (SE Italy).

The Numidian has a long history of sedimentological and stratigraphic research (reviewed by Thomas et al., 2010), recently recast as a structurally-confined turbidite system (Pinter et al., 2016; 2017). It is this that is responsible for the characteristically fractionated grain-sizes in deposits, with fairways marked by thick, amalgamated generally well-sorted medium-to-coarse sandstones as distinct from thin-bedded fine sandstones, siltstones and claystones. In most literature, the biostratigraphic age of the Numidian has been poorly constrained within a late Oligocene-mid Miocene bracket. This uncertainty is common for turbidites which tend to rework basin floor sediments. However higher-resolution calcareous biostratigraphy linked to detailed sedimentary logs has established the age of Numidian sandstones on Sicily to be late Aquitanian to Langhian in age (Pinter et al., 2017).

Our case study comes from the thrust belt of Central-East Sicily (Fig. 1a-b), broadly within the same setting as the Gagliano gas field (about 10 km eastward; Carbone et al., 1990; Pieri and Mattavelli, 1986). The Numidian strata here lie stratigraphically upon Cretaceous-Oligocene deep-water mudstones (Figs. 1b). The Numidian, cropping out in the area, is mainly composed of brown clays and sandstones (quartz-arenites) of Burdigalian age (Pinter et al., 2017). The sandstones are amalgamated deposits with composite thicknesses in excess of 50m in places. The full succession can reach thickness of over 1500m in the area (Pinter et al., 2017). However, at the village of Sperlinga (Fig. 1), the full Numidian succession is just 250m thick, capped by siliceous marlstones (so-called "silexites", Broquet, 2016 and reference therein). These marlstones chart the termination of deposition at this locality of the turbidite sandstones, indicating a switch in sediment dispersal pathways in the basin.

Pinter et al. (2017) interpret the stratigraphic thickness variations as representing deposition in embryonic thrust-top basins, a setting consistent with the general interpretation of the depositional system as structurally-confined. The Sperlinga section represents a marginal part of a sedimentary wedge within a thrust-top basin, as it onlaps southwards onto an ancestral thrust anticline. Thicker successions elsewhere represent depocentres within synclines. These thicker units, in the nearby Nicosia area yielded low estimates of palaeothermal maxim (R0 mixed layers illite-smectite with an illite content ≤60%, and vitrinite reflectance values ≤ 0.5% VRo%; Di Paolo et al., 2014). These suggest a sedimentary burial depth < 2 km. The sedimentary thickness in Sperlinga is only 300 m and the succession likely rather low sedimentation away from the main siliciclastic input in the area (Lentini et al., 1996; Pinter et al., 2017). Consequently, even if erosion could have occurred, sedimentary burial was probably less than 1 km. The area has not been buried subsequently by thrust sheets. Any overlying, younger Miocene strata are unlikely to have exceeded a thickness of more than 1 km. These regional constraints provide a maximum burial depth for the Sperlinga section.

The Sperlinga area has been carried by lower structures within the thrust wedge of the Maghrebian system, and consequently has experienced a c 100° CW rotation since deposition (Speranza et al., 2003). It contains sub-vertical, NW-SE striking sandstone ridges that provide around 100m relief in the surrounding countryside. These ridges are the limbs to a tight syncline (Fig. 1c) with km-scale wavelength and the sub-vertical beds contain multi-scale deformation bands that form complex networks. They are the focus of this study.

3. Methods

3.1 Scan-line and scan-area sampling

Data on deformation bands were collected using several different methods, applied to five outcrops within our study area (Fig. 2). In literature four main sampling strategies for collecting fracture data are widely used (see Watkins et al., 2015 for a review): i) the linear scanline method (Priest and Hudson, 1981; Priest, 1993); ii) areal sampling (Wu and Pollard, 1995); iii) rectangular window sampling (Pahl, 1981; Priest, 1993); and iv) the circular scanline method (Mauldon et al., 2001; Rohrbaugh et al., 2002).

We adopted the linear scanline (Priest and Hudson, 1981; Priest, 1993) and window sampling methods (Pahl, 1981; Priest, 1993) because our goal is the definition of attributes such as orientations, lengths frequency, and thickness.

A combination of linear scanlines and areal sampling were used. For scanlines the following attributes were measured: strike, dip, apparent displacement, and size (thickness, length, and spacing). As regarding deformation bands length, data reported here, are to be considered "semi-lengths", which is the half-length measured above or below the scan-line; this approach applied to all structures does not compromise the statistical analysis as a whole. The maximum semi-length was set at 5m (Hc); deformation bands with semi-lengths longer than 5m are reported as ">Hc". For these longer deformation bands and those with separations greater than tens of metres (up to tens of meters spacing), the application of scanline method is not practical. For these we adopted an *ad hoc* approach and were only able to estimate their spatial orientation and approximate spacing (Fig. 3a).

Our study is limited to five specific sites because of access restrictions. However, these provide good coverage of the fold structure that is our objective. These contain a variety of orientations of outcrop faces that provide quasi 3D contexts for deformation band characterisation.

3.2 Petrography and petrophysics

In order to characterise the microstructures, we performed a set of different analyses on a suite of selected specimens. Petrographic investigation was carried out on thin sections prepared from such samples. Mineral chemistry, density contrast maps (electron back scattered images) and microstructural analyses were created using a EPMA (CAMECA SX-100) at TU Clausthal (Germany) with an electron beam in the range 5-30 keV.

Porosimetry was carried out with Thermo scientific® mercury porosimeters (Pascal 140 and 240 models) at the University of Catania. With mercury intrusion porosimetry, the determination of pore size is based on the properties of non-wetting liquids in capillaries. The relation (Eqn.1) between pore size and applied pressure assuming cylindrical pores is expressed by the Washburn equation (Drake, 1949).

$$P\,r = -2\gamma\cos\phi, \qquad \text{(Eqn. 1)}$$

where r is the pore radius, ϕ - surface tension of mercury, γ - contact angle, P - applied absolute pressure.

This equation permits the determination of the total cumulative volume of pores and the volume of pores referred to dimensions, together with the porosity (expressed as the ratio between pore volume and the external sample volume). The Pascal 140 porosimeter was used for low pressure measurements (below 100 kPa) while the Pascal 240 for measurements up to 200 kPa. Collectively this allows the smaller pores to be detected. The mercury porosimetry technique allows density of the studied specimens to be measured. We used SOL.I.D (Solver of Intrusion Data) software for computation of data obtained from mercury porosimetry.

3.3 X-ray microtomography

Two selected samples with size of about 4 mm were imaged at the SYRMEP beamline of the Elettra synchrotron light source (Trieste, Italy) in *white-beam* configuration mode at high spatial resolution. The X-ray spectrum was filtered for low energies with 1 mm of Si + 1 mm of Al, and the sample-to-detector distance was set to 200 mm. For each measurement, 1800 projections were acquired over a total scan angle of 180° with an exposure time/projection of 2 s. The detector consisted of a 16 bit, air-cooled, sCMOS camera (Hamamatsu C11440 22C) with a 2048 × 2048 pixels chip. The effective pixel size of the detector was set at 1.95^2 μm^2, yielding a maximum field of view of ca. 3.2^2 mm^2. Since the lateral size of the samples was larger than the detector field of view, the microtomographic scans were acquired in local or region-of-interest mode (Maire and Withers, 2014). A single distance phase retrieval pre-processing algorithm (Paganin et al., 2002) was applied to the white beam projections, in order to improve the reliability of quantitative morphological analysis and enhance the image contrast.

4. Outcrop scale structure

The area is characterized by steeply inclined to upright folds, with km wavelengths and sub-horizontal hinge lines that trend NW-SE.). Access to the outcrops is via walkways and battlements of the village's Norman castle – the carved bedrock walls provide unique multi-2D views of the deformation bands. All sampling was carried out with permission, using debris from the 2015 rock falls. Scanlines and other non-destructive measurements were carried out on *in situ* materials.

The deformation bands studied here (Figs. 3-6) all come from the sub-vertical to steeply overturned southern limb of a syncline and are hosted in thick-bedded quartz-sandstones. The sandstones are poorly quartz-cemented and, locally, highly friable and incoherent. The most prominent set, more than 5 mt in length (up to 50 mt; >Hc on Figs. 2, 5), dipping about 55° to the NW, with an average spacing of ca. 10 mt, is visible along the southern flank of Sperlinga syncline below the castle (Fig. 3a). In outcrop, such structures appear as brownish-red discontinuities with a general positive relief (Fig. 3b).

A network of smaller, commonly conjugate deformation bands also occur (Figs. 3b, 4b-d). This set, also red in color and with a positive relief, have lengths of between 0,5 and 1 meter and commonly, a decimetre spacing. Locally, deformation bands evolve towards their terminations to joints and fractures (Fig. 3c; see description of site 2, in the next chapter).

Accessing the castle, along the main corridor, an anastomosing suite of deformation bands (Fig.4a), sub-parallel to bedding, forms a particularly prominent set, with associated extensive braided arrays. This is the best developed suite and is cross-cut by the previously described suites that are at a higher angle to bedding (Fig. 4b).

5. Sampling sites

To characterise the suites of deformation bands, their relationships to each other and their population statistics, we chose different sampling sites on the basis of outcrop excellence and accessibility. Five selected sites for detailed structural investigation are located along the steep SW limb of the Sperlinga syncline (Fig. 2). We now describe each of these in turn.

Site 1 (Figs. 2, 6a) gives us a good opportunity of looking at the relationship between the main sets of deformation bands. On the basis of the outcrop analysis, we recognized 6 sets of deformation bands, mainly distinguished by length and orientation, as reported in Fig. 6a. This geometry defines a hierarchical relationship among them: the main set (set 1, red on Fig. 6a) is represented by longer deformation bands (which usually show higher offsets), while other deformation bands show smaller lengths and an abutting termination on the main set. Similarly, set 1 is, in turn, subordinated to the most prominent one (tens of meters-spaced; >Hc on Fig. 2) dipping to the NW previously described. Length/spacing ratio indicates a positive linear relation (inset of Fig. 6a), which suggests a unique evolving deformation event for the observed sets.

Site 2 (Figs. 2, 3d) is located at the base of one of the aforementioned sandstones ridges. At this site, red coloured poles on Fig. 2 show joints distribution (St2, n=56) in addition to a few deformation bands data (St2, n=7). Here, fracturing took place on pre-existing deformation bands. Joints exhibit a relatively smooth surface, no displacement, and a mean aperture of about 2-3 mm, only few of them are open joints with aperture up to 25 mm characterized by muddy filling derived from the soil layer above.

Site 3 (Fig. 2) is located in the south-easternmost area of Sperlinga village. The main cluster of poles occurs in the southeastern quadrant giving a mean plane moderately dipping (ca. 50°) towards NW.

In Site 4 (inside the castle; Figs. 2, 4a-d), we also recognized a 50 cm-thick, white cluster zone of multiple deformation bands (75/60 - Dip/Dip Direction) running along the ridge; this is cut and offset (34 cm on left) by a >Hc deformation band (60/33 - Dip/Dip Direction). Beside the most frequent orientation (cluster in the SE quadrant) further data lie in NW quadrant (and subordinately in the NE and SW quadrants) forming a conjugate system. These are short deformation bands (few of them exceed 1m) and cross-cut the white band. Aligned with the band there are some ellipsoidal boulders (30-70 cm long; Fig. 4a-b) with long axes oriented in the same direction (strike) of bedding.

In Site 5 (Figs. 2, 6b), using scan-area setup (2.80 x 2.00 m), we performed a more detailed analysis on short deformation bands (few cm length and few mm spacing; Fig. 5a); data obtained confirm the main cluster on SE quadrant (as reported on the other stations) and secondary clusters on NE and SW quadrants, comparable with St4 (Fig. 2).

Scan-lines show a main frequency peak of deformation bands ranging between 0,5 and 1 metre (Fig. 5a). Thickness values range from 1 mm to 5 mm (although 2 mm is typical) and no evident relationship exists between thickness and length (see Appendix A). Only a few deformation bands show a clear sense of shear; displacement is usually limited, ranging from 1 cm to 7 cm but a maximum of 34 cm (left lateral) offset is recognised on a horizontal scan-line (St4). Higher displacements are generally recognised on longer deformation bands (>Hc), and a weak direct relationship between length and displacement is observed within the population as a whole (Fig. 5b).

Our study reveals two broad suites of deformation bands within the steep fold limb. One set is sub-parallel to bedding and forms an elongate anastomosing network. This system is cross-cut by smaller clusters and individual deformation bands that lie at a high angle to bedding.

These sets of structures can be related to the distribution of both deformation bands and fractures across sandstone folds (Świerczewska and Tokarski, 1998; Cosgrove and Ameen, 2000). In particular, the high-angle smaller cluster can be associated to two sets of conjugate shear fractures (Watkins et al., 2015) with an acute bisector perpendicular to the fold hinge, whereas the anastomosing set can be related to a joint set striking sub-parallel to the fold hinge in fold and thrust belt (Price and Cosgrove, 1990).

6. Petrography and microstructures

6.1 Petrography

Quartz is the most abundant mineral (> 99 vol%) forming, with clasts of various dimensions (mean grain-size 0.3 – 0.5mm). The whole rock has a general grain-bearing framework with a lower amount of quartz cement and iron deposits. Other constituting phases are: opaque minerals (illite, rutile), glauconite, alkali-feldspar, zircons, monazite and white-mica (Fig. 7; Table 1). The grain-size appears heterogeneous (ranging from medium to very coarse sand) resulting in a moderately sorted sediment (except for SPR4 that shows a certain homogeneity), even though a mean dimension of 0.3 – 0.5 mm is dominant. Roundness and sphericity show a high variation; clast external morphology ranges from sub-angular to well-rounded. Quartz grains vary from mono- to poly-crystalline. Some larger clasts (of either type) contain fractures.

Minor (probably detrital) glauconite is found in all samples, with a grain size ranging from 50 μm to 500 μm, showing a sub-rounded to rounded shape, even though, sometime, grains are broken in smaller pieces. In thin sections colour varies from brownish-green to green and from pale to dark-green but dark and intense green is definitively more common. Almost all glauconite grains show a high pleocroism on green absorption tones. Despite the optical characteristics are typical of glauconite, chemical analyses carried out with EPMA suggest a more complex nature, consisting of chlorite, glauconite and an Al-rich phase (Tab.1). The sandstones contain rare feldspar grains. These are exclusively K-feldspar ($Kfs_{89-96}Ab_{11-4}$). Commonly they are broken and some grains are highly weathered (Fig. 7e). Few detrital zircons occur in all the studied samples. Grain size ranges from 30 μm to 500 μm. Grains are commonly ovoidal even though some are rounded or cuboid.

6.2 Microstructures

Four specimens have been studied via EPMA (SPR1, SPR2, SPR3, and SPR4). SPR1 (collected on site 4) is characterized by a cross-cutting 1.5 mm thick, brownish deformation band (Fig. 8a) that shows a higher grain-compaction grade (Figs. 8b-c). The brownish-red colour is due to an iron rich matrix (*Limonite s. l.*). In the host rock, the structure is grain-supported and no matrix is recognized; a weak quartz-grains shape orientation, perpendicular to the deformation band is observed. Within the band, porosity reduction is observed; it results from pore-collapse and iron-rich deposit filling (the latter might also indicates permeability decrease through the deformation band). These features suggest a compaction nature of the deformation band without shear component (Fig. 8).

SPR2 contains a 2 cm-thick deformation band with a positive profile on the outcrop wall (collected on Site 3). Here, we recognised two parallel deformed portions (Fig. 9a); the first one is characterized by brownish-red, iron-rich matrix and coarser grain-size (Fig. 9b), while the second one is recognizable by a marked anisotropy and finer grain-size (Fig. 9c-d).

Anisotropy is due to the presence of some closely spacing sub-parallel deformation bands, whose thickness range from 0.5 mm to 2 mm (Fig. 9). The structure appears grain-supported in the host rock where porosity is relatively reduced (compared with other specimens) and becomes matrix-supported within the micro-deformation bands; here, primary porosity and grain-size are further reduced and matrix results from grain crushing processes (cataclasis – Fig. 9c). Extensional fractures can be observed into the deformation bands (Fig. 9c-d). Fractures show an *"en echelon"* geometry indicating an incipient shear surface. Some deformation bands show a complete coalescence of such "*en echelon"* fractures forming a continue shear surface (labelled "shear band 2" on

Fig. 9c). Moreover, within the bands some rounded clasts suggest grain-rotation kinematics (Fig. 10 a-b).

Within the brownish-reddish deformation bands, iron-rich matrix filling contributes to a porosity reduction; anyway a certain grade of porosity is maintained (Fig. 9b). In such domain, no shear indicators have been detected.

In SPR3 specimen (collected on Site 4), the transition from the undeformed portion to the deformation band is gradual. It can be recognized by looking at the colour, matrix content and structure variations through the thin-section (Fig. 10c). A grain-supported, light coloured and coarse structure becomes darker, more compacted and finer, moving toward the deformation band. This change results in a porosity reduction into the deformation band (Fig. 10c). Porosity decrease is mainly due to compaction, and matrix contributes to a complete pore-filling. No kinematic indicators have been found.

SPR4 (collected on Site 4) represents an undeformed volume (host rock) with no evidence of deformation structures; it shows a homogeneous and fine grain-size ranging from 200µm to 500µm. The structure is generally grain-supported even if locally, a higher matrix amount could be observed.

On the basis of microstructural observation, two groups of deformation bands are identified:

1) compaction bands; characterized by compaction, iron-matrix, coarser grain-size, up to 5 mm thickness and no clear evidence of shear.

2) shear bands; characterized by local grain-rotation, cataclastic matrix core, 0.5-1 mm thick, and, in some instances, formation of a discrete slip surface due to coalescing en-echelon fractures. These features allowed us to further classify shear bands as "slipped deformation bands" (Rotevatn et al. 2008)

7. X-ray micro-CT and Hg porosity measurements

X-ray computed microtomography (X-Ray micro-CT) have been performed on representative specimens of both compaction and slipped deformation bands as well as on host rock. X-Ray micro-CT data are reported in Fig.11 and Tab.2.

SPR1 shows a porosity decrease within the compaction band (6.75%) compared to the host rock (17.9%) as inferred by microscopic observation (Tab. 2). The porosity reduction results from compaction mechanism and iron-rich deposit (Fig. 11a).

In SPR2, measurements were performed at the limit between compaction band (brownish-red volume) and micro-deformation band (Fig. 11b). Results highlight a porosity value of 3.90% (which is quite consistent with what observed in SPR1), and 0.86% within the micro-deformation band (Tab. 2). The latter, is in agreement with microscopic observation, where reduced porosity is associated with the presence of cataclastic matrix. SPR4, considered as a representative host rock volume without deformation bands, shows a porosity value of 26.46 % (Tab. 2).

We also compared X-ray micro-CT data with mercury porosimetry tests (Fig. 12), that have been carried out on two specimens, considered to be representative of either host rock (SPR4) and deformation bands (SPR1; Tab. 3). Unfortunately, because of the low mechanical features, it was not possible to carry out porosimetry analyses on the micro-Deformation bands.

Results confirmed that the two portions are characterised by different porosity values, higher in the host rock (26.75%) than in the compaction band (15.95%). This, despite the pore size is larger in the host rock compared to the deformation band, where pre-existing pores are often filled and therefore poorly connected as also noticed by petrographic observation. Moreover, in the host rock pores seem to belong to a narrow size range, whereas in the deformed band they belong to various size classes (Fig. 12).

8. Discussion

Our multiscale investigation characterised an outcrop analogue of gas reservoir in Sperlinga Numidian sandstones in central eastern Sicily where deformation band arrays relate to folding. Our study concentrates on the limb of a tight, upright syncline. There are two main sets of deformation band – the main best-developed set is sub-parallel to bedding (Fig. 13). We assume that this array represent incipient bed-parallel thrusting before amplification of the Sperlinga syncline, although it might alternatively accommodated flexural flow during folding. Both explanations satisfy the NE-side-up kinematics of these structures. These early deformation bands are overprinted by secondary arrays that form broadly conjugate sets, where the left-lateral set evolved more than the other (Fig. 14). The acute bisector of these arrays is sub-perpendicular to the fold axis, so sub-parallel to the inferred direction of maximum contraction.

The general pattern of deformation band sets at Sperlinga are broadly consistent with models for jointing during folding of competent rocks such as limestones (e.g. Cosgrove and Ameen, 2000; Awdal et al., 2016). It is interesting that the structures at Sperlinga show these simple relationships to the host syncline. They do not betray any of the rotational strain history for the thrust belt detected paleomagnetically (Speranza et al., 2003) which we deduce must have, at least locally, been accommodated without distortional strain of the thrust wedge.

The Sperlinga site was chosen to be representative of deformation under low-burial conditions. They are both of compaction and shear-type, using the classification of Aydin et al. (2008) - and show the effects of grain boundary sliding and compaction with minor cataclasis (Figs. 8, 9b-c); it is further highlighted by abrasion of the corners of angular grains during granular sliding (Fig. 9c). Grain-crushing is generally inferred to act under confining pressures equating to burial in excess of 1 km (e.g. Fisher and Knipe, 2001). However, we can rule out significant burial for the Sperlinga section. It is possible that the cataclasis described here reflects reactivation of inherited fractures within the sedimentary grains, so that the grain-strengths based on single-crystal, flawless quartz is over-estimates. Alternatively strain-rate and loading conditions for the Numidian sandstone – deformed by folding – may not have been comparable with those inferred for fault damage zones.

Multi-technique petrophysical analyses revealed their internal structure and porosity micro-connectivity impact on the performance of these types of strata as hydrocarbon reservoirs.

High resolution images and mercury porosimetry allowed us to qualitatively and quantitatively estimate the porosity and grain-size variations as well as microstructures, and the reduced porosity with respect to the host rock. Compaction bands are definitely more common; they result in a porosity reduction and an iron-rich matrix filling, which produces a permeability reduction. Slipped deformation bands are accompanied by cataclastic processes resulting in a grain-size and porosity reduction (because of cataclasis matrix). Within the slipped deformation bands, extensional *en-echelon* microfractures are observed (Figs. 9c-d, 10b) and, in some instances, coalescing *en-echelon* fractures produce a continue shear surface.

Therefore, from a microstructural point of view, compaction bands are expected to behave as a fluid barrier, whereas the presence of extensional and shear fractures within the slipped deformation bands should represent a preferred way for fluid/gas phases.
As with other emergent thrust systems, early-burial folding in the thrust wedge of Sicily is common, as evidenced by widespread preservation of syn-kinematic strata in growth synclines (Butler and Lickorish, 1997; Butler et al., 2015). Deformation sequences are known to be complex, with distributed folding occurring in parallel to displacements on major thrusts. Therefore, deformation band arrays formed within a few hundred metres of the Earth's surface, such as those described here, are to be expected. This damage will be incorporated, along with depositional heterogeneity and early diagenetic effects, to influence petrophysical properties when these rocks become buried. This burial can happen when break-back or continued thrust activity emplaces substrate over thrust top basin fills. Early burial damage, through arrays of deformation bands, may be commonplace in emergent thrust systems elsewhere.

9. Conclusions

The combination of field structural investigations and detailed meso- and micro-structural analyses gives us a comprehensive picture of an outcrop analogue, in the Sperlinga Numidian sandstones, of a sub-surface gas reservoir in Gagliano. These types of successions with their structural heterogeneities are important exploration targets in other compressional settings, especially those on deepwater continental margins. Therefore, our study can be informative in several cases.

At least, two main deformation stages are here observed. The last and more prominent one (NE-SW oriented) has been formed by the evolution of left-lateral set of conjugate deformation bands sets (Figs. 3b, 13b, 14c).
A continued deformation event will eventually produce fractures (or faults) on the pre-existing deformation bands (Fig. 3c). In studied sandstones, qquartz constitutes almost the whole rock mineralogy and forms a grain-bearing structure with a lower amount of quartz-cement.

Two main types of deformation bands are here observed: compaction and shear bands. The latter ones show grain-crushing and fracturing processes within the deformation bands leading formation of discrete slip surface.
Porosity analyses highlight a value of about 26% for the undeformed rock (host rock). This value is reduced within the compaction bands (3.90-6.75%) and further reduced (0.86%) within the shear deformation bands.

The main important points derived from the study are listed below:

- The work depicts how folding, at shallow burial depth, may generate deformation bands in deep-water sandstones.

- The role and geometry of deformation bands sets, related to a syncline fold developed into a thrust system, is broadly consistent with models for jointing during folding (Figs. 3, 14).

- Arrays spatial orientation of multiple sets of deformation bands are crucial to simulate and model 3D flow channelling within a porous medium. They can act both as channels or rather as barriers influencing fluids migration (gas, oil). Their full characterization is of great importance in the management of field gas production.

- Our findings suggest that compaction band developed in sandstones are characterized by lower porosity with respect to host rock, as usually expected, whereas shear-type bands are preferential pathways for fluids especially when they coalesce and evolve to fractures.

Acknowledgements

We really appreciated the criticisms and valuable observations by two anonymous reviewers which improved significantly an early version of the manuscript. We are grateful to Prof. Kurt Mengel for availability to perform microanalysis with EPMA facility at TU Clausthal (Germany) and Totò Scalisi and the Major of Sperlinga village to permit access to the castle. SG acknowledges an Erasmus+ grant funded by the University of Catania. EF, RM and RP acknowledge a FIR 2014 CF093A grant from the University of Catania (Scientific Coordinator R. Maniscalco). EF, RP are thankful to Lucia Mancini for help and assistance during X-ray tomography acquisitions.

References

- Aydin, A., Johnson, A., 1978. Development of faults as zones of deformation bands and as slip surfaces in sandstone. Pure and Applied Geophysics, 116, 931-942.
- Aydin, A., Borja, R.I. and Eichhubl, P., 2006. Geological and mathematical framework for failure modes in granular rock. Journal of Structural Geology, 28, 83–98.
- Awdal, A., Healy, D., Alsop, G. I., 2016. Fracture patterns and petrophysical properties of carbonates undergoing regional folding: A case study from Kurdistan, N Iraq. Marine and Petroleum Geology, 71, 149-167.
- Bianchi, F., Carbone, S., Grasso, M., Invernizzi, G., Lentini, F., Longaretti, G., Merlini, S., Mostardini, F., 1987. Sicilia orientale: profilo geologico Nebrodi-Iblei. Mem. Descr. Soc. Geol. It., 38, 429-458.
- Butler, R.W.H., Lickorish, H., 1997. Using high-resolution stratigraphy to date fold and thrust activity: examples from the Neogene of south-central Sicily. Journal of the Geological Society, London, 154, 633–643.
- Butler, R.W.H., Maniscalco, R., Sturiale, G., Grasso, M., 2015. Stratigraphic variations control deformation patterns in evaporite basins: Messinian examples, onshore and offshore Sicily (Italy). Journal of the Geological Society,172 (1), 113.
- Broquet, P., 2016. Sicily in its Mediterranean geological frame. Boletín Geológico y Minero, 127 (2/3), 547-562.
- Carbone, S., Catalano, S., Grasso, M., Lentini, F. and Monaco, C., 1990. Carta geologica della Sicilia centro-orientale. Scala 1:50.000. S.EL.CA., Firenze
- Cosgrove, J.W., Ameen, M.S., 2000. A comparison of the geometry, spatial organization and fracture patterns associated with forced folds and buckle folds. Cosgrove J.W and Ameen M.S. (Eds.) Forced folds and fractures. The Geological Society London.

- Di Paolo, L., Olivetti, V., Corrado, S., Aldega, L., Balestrieri, M.L., Maniscalco, R., 2014. Detecting the stepwise propagation of the Eastern Sicily thrust belt (Italy): insight from thermal and thermochronological constraints. Terra Nova 26, 363–371. doi: 10.1111/ter.12106
- Drake, L.C., 1949. Pore-size distribution in porous materials. Ind. and Eng. Chem., 780–785.
- Elter P., Grasso M., Parotto M., Vezzani L., 2003. Structural setting of the Apennine-Maghrebian thrust belt. Episodes, 26 (3), 205-211.
- Farrell, N.J.C., Healy, D., Taylor, C.W., 2014. Anisotropy of permeability in faulted porous sandstones. Journal of Structural Geology, 63, 50-67.
- Fisher, Q.J., Knipe, R.J., 2001. The permeability of faults within siliciclastic petroleum reservoirs of the North Sea and Norwegian Continental Shelf. Marine and Petroleum Geology 18, 1063–1081
- Fossen, H., Schultz, R. A., Shipton, Z. K., Mair, K., 2007. Deformation bands in sandstone: a review. Journal of the Geological Society, London, 164, 755–769.
- Fossen, H., Soliva, R., Ballas, G., Trzaskos, B., Cavalcante, C., Schultz, R.A., 2017. A review of deformation bands in reservoir sandstones: geometries, mechanisms and distribution. In: Ashton, M., Dee, S. J. and Wennberg, O. P. (Eds) Subseismic-Scale Reservoir Deformation. Geological Society, London, Special Publications, 459, https://doi.org/10.1144/SP459.4
- Jamison, W.R., Stearns, D.W., 1982. Tectonic deformation of Wingate Sandstone, Colorado National Monument, Bull AAPG, 66, 2584-2608.
- Johansson, M., Braakenburg, N. E., Stow, D.A.V., Faugeres, J.C., 1998. Deep-water massive sands: facies, processes and channel geometry in the Numidian Flysch, Sicily. Sedimentary Geology, 115, 233-265.

- Lentini F., Catalano S., Carbone S., 1996. The external thrust system in southern Italy: A target for petroleum exploration. Petroleum Geoscience, 2 (4), 333-342.
- Maire, E., Withers, P.J., 2014. Quantitative X-ray tomography. Int. Mater. Rev., 59, 1-43.
- Mauldon, M., Dunne, W.M., Rohrbaugh, M.B., 2001. Circular scanlines and circular windows: new tools for characterizing the geometry of fracture traces. Journal of Structural Geology, 23, 247-258.
- Paganin, D., Mayo, S.C., Gureyev, T.E., Miller, P.R., Wilkins, S.W., 2002. Simultaneous phase and amplitude extraction from a single defocused image of a homogeneous object. J. Microsc.-Oxford 206, 33-40.
- Pahl, P.J., 1981. Estimating the mean length of discontinuity traces. Int. J. Rock Mech. Min. Sci. Geomech. Abstr. 18, 221-228.
- Pieri, M., Mattavelli, L., 1986. Geologic framework of Italian petroleum resources. Bull. Am. Assoc. Petrol. Geol. 70, 103-130.
- Pinter, P. R., Butler, R.W.H., Hartley, A.J., Maniscalco, R., Baldassini, N., Di Stefano, A., 2016. The Numidian of Sicily revisited: a thrust-influenced confined turbidite system. Marine and Petroleum Geology, 78, 291-311.
- Pinter, P. R., Butler, R.W.H., Hartley, A.J., Maniscalco, R., Baldassini, N., Di Stefano, A., 2017. Tracking sand-fairways through a deformed turbidite system: the Numidian (Miocene) of Central Sicily, Italy. Basin Research, 1–22, doi: 10.1111/bre.12261.
- Price, N.J. & Cosgrove, J.W., 1990. Analysis of Geological Structures. Cambridge Univ. Press. 502 pp.
- Priest, S.D., 1993. Discontinuity Analysis for Rock Engineering. Chapman & Hall, London, United Kingdom.
- Priest, S.D., Hudson, J.A., 1981. Estimation of discontinuity spacing and trace length using scanline surveys. Int. J. Rock Mech. Min. Sci. Geomech. Abstr., 18, 183-197.

- Rotevatn, A., Torabi, A., Fossen, H., Braathen, A., 2008. Slipped deformation bands: A new type of cataclastic deformation bands in Western Sinai, Suez rift, Egypt. Journal of Structural Geology, 30, 1317–1331.
- Rotevatn, A., Fossen, H., 2011. Simulating the effect of subseismic fault tails and process zones in a siliciclastic reservoir analogue: Implications for aquifer support and trap definition. Marine and Petroleum Geology, 28, 1648-1662.
- Saillet, E., Wibberley, C.A.J., 2013. Permeability and flow impact of faults and deformation bands in high-porosity sand reservoirs: Southeast Basin, France, analog. Bull. Am. Assoc. Petrol. Geol., 97, 437-464.
- Schultz, R. A., Siddharthan R., 2005. A general framework for the occurrence and faulting of deformation bands in porous granular rocks. Tectonophysics, 411, 1 – 18.
- Speranza, F., Maniscalco, R., Grasso, M., 2003. Pattern of orogenic rotations in central-eastern Sicily: implications for the timing of spreading in the Tyrrhenian Sea. Journal of the Geological Society, 160, 183-195.
- Swierczewska, A., Tokarski, A.K., 1998. Deformation bands and the history of folding in the Magura nappe, Western Outer Carpathians (Poland). Tectonophysics, 297, 73-90.
- Thomas, M.F.H., Bodin, S., Redfern, J., Irving, D.H.B., 2010. A constrained African craton source for the Cenozoic Numidian Flysch: Implications for the palaeogeography of the western Mediterranean basin. Earth-Science Rev., 101, 1–23. https://doi.org/10.1016/j.earscirev.2010.03.003.
- Watkins, H., Bond, C.E., Healy, D., Butler, R.W.H., 2015. Appraisal of fracture sampling methods and a new workflow to characterise heterogeneous fracture networks at outcrop. Journal of Structural Geology, 72, 67-82.
- Wezel, F.C., 1970. Numidian Flysch — an Oligocene – Early Miocene continental rise deposit off African platform. Nature, 228 (5268), 275–276.

- Wu, H., Pollard, D.D., 1995. An experimental study of the relationship between joint spacing and layer thickness. Journal of Structural Geology, 17, 887-905.

Figure captions

Fig.1. (a) Geological map of central-East Sicily (Pinter *et al. 2017.* modified after Carbone *et al.*. 1990). (b) Regional tectonic scheme. (c) Geological section A-A' traced on (a).

Fig.2. Geological-structural map of the Sperlinga-Nicosia Area (modified after Carbone *et al.*.. 1990. and Pinter *et al.,* 2017) showing locations of field investigation sites (1-6) and related stereoplots (lower hemisphere. equal-area projections). All the poles are related to DBs except for Site 2 (which represent joints) and Site 6 (which represent bedding).

Fig.3. Photos showing multi-scales generations of DBs. (a) Photo of the Sperlinga sandstone ridge showing long-spacing DBs (referred as major); on top the Norman castle. (b) Meter-scale. Conjugate DBs on front of the Sperlinga Castle. (c) Evolution of DBs into fractures. (d) Photo showing sandstone grain-size and iron-oxide focused within DBs.

Fig.4. Photos showing the interior of the Sperlinga castle (Site 4). (a) External corridor showing boulders alignment and a white deformation band cluster zone. (b) Detail of a long-scale DBs offsetting (34mm left-lateral) the 50 cm-thick DBs cluster zone (red-plane indicates one left-lateral DB surface). (c) Detail of cross-cut relation of major DBs on the front of the sandstone ridge. (d) Photo from the inside of the Sperlinga castle showing DBs multi 2D-spatial orientation.

Fig.5. (a) DBs semi-length/frequency diagram. Image shows a higher frequency of structures with semi-lengths between 0.5 m and 1 m. (b) Semi-length/offset diagram showing a slight linear positive relationship.

Fig.6. Image showing the hierarchical relationship of DBs (relative to the most evident deformation). DBs are generally limited and subordinate to longer and higher spaced DBs. Length/Spacing ratio shows a linear relation suggesting a unique deformation event for these sets.

Fig.7. BSE images of typical accessory minerals in Numidian quartz-arenites. (a) Glauconite (Glt). (b) Zircon (Zrn). (c) Ilmenite (Ilm). (d) Rutile (Rt). (e) Alkali-feldspar (Kfs). (f) White-mica (Wm).

Fig.8. SPR1 photo (left) and DB details. Centre: DB detail showing brownish-red matrix filling inter-granular pores (OM parallel polarized image). Right: BSE image of the previous detail. Image shows a porosity (black) reduction and an iron-rich deposit (white) within the DB.

Fig.9. SPR2 and DBs details: (a) scan of entire thin section; (b) compaction band domain. Image shows a higher iron-rich deposit amount; (c) slipped deformation bands domain. Image shows a finer grain-size within the slipped deformation bands produced by cataclastic processes (e.g. grain crushing) and a coarse grain-size outside. Within the slipped deformation bands some en-echelon fractures produce, when coalescing, a continue slip surface; d) detail of en echelon fractures within the slipped deformation bands.

Fig.10. (a) Optical microscope image showing micro-fractures within the Slipped DB. (b) Interpretation. OM image shows en-echelon extension fractures (red dashed lines) and compression domains (black dashed lines) indicating a right sense of shear (to be considered as left on outcrop). (c) SPR3 epoxy blue-resin thin-section. Image shows a gradual porosity decrease toward the compaction DBs. Porosity is almost completely filled within the compaction band.

Fig.11. 3D-volumetric rendering of specimens analysed by means of X-ray micro-tomography: (a) SPR1 shows a higher porosity (red) within the host rock and a higher iron-deposit amount (green) within the deformed volume (upper part); (b) SPR2 compaction band (upper part) shows an increase of iron deposits. Slipped deformation band (bottom part) characterized by finer grain size (grain-crushing).

Fig.12. Micro-porosimetric analysis. (a) Host rock manifest higher porosity (as reported in tab.3) and. pore-size seems to belong to a single size-class (24 nm). (b) Within the compaction band porosity decreases and pore show various size-classes.

Fig.13. 3D-sketch - not in scale - summarizes the main features observed at outcrop scale showing the distribution, orientation and cross-cutting relations of deformation bands within the

overturned southern limb of Sperlinga syncline (grey arrows indicate the direction of maximum contraction; f. a.= fold axis).

Fig.14. Deformation stages. (a) Early stage might have created sets of DBs which were overprinted and partially obliterated during following stages. (b) Incipient bed-parallel thrusting before amplification of the Sperlinga syncline has formed DBs cluster zone visible on top of the fold. (c) Continued deformation formed broadly conjugate sets (offsetting the DBs cluster zone). Left-lateral set evolved much more than the right-lateral and has formed the major DBs (black thick lines).

Tables

Table 1. Chemistry (oxides expressed as Wt %) of accessory minerals by mean of EPMA.

Mineral	Na_2O	MgO	Al_2O_3	SiO_2	K_2O	CaO	TiO_2	FeO	Cr_2O_3	MnO	ZrO_2	HfO_2	Total
	2.19	7.01	33.53	35.74	0.06	0.38	1.05	7.09	0.04	-	-	-	87.10
	1.64	6.66	35.3	35.29	0.07	1.12	0.71	7.08	0.06	-	-	-	87.94
Glauconite	1.72	7.1	35.04	36.02	0.03	0.85	0.9	6.14	0.06	-	-	-	87.85
	1.95	6.08	34.01	35.88	0.04	0.23	0.7	8.15	-	0.19	-	-	87.24
	1.68	2.75	34.93	34.96	0.05	0.19	0.35	12.2	-	0.13	-	-	87.25
	0.77	-	19.34	63.76	15.7	0.09	0.02	0.12	-	0.02	-	-	99.83
	0.45	-	19.17	63.53	16.14	0.06	0.02	-	-	-	-	-	99.37
Alkali-Feldspar	0.76	-	19.29	62.75	15.27	0.01	-	0.06	-	-	-	-	98.14
	0.83	-	18.96	63.5	15.39	0.03	-	0.01	-	0.02	-	-	98.75
	0.56	-	19.25	63.86	15.87	0.06	-	0.02	-	-	-	-	99.62
	0.49	0.69	37.22	46.07	9.64	0.01	0.82	1.19	-	-	-	-	96.12
	0.46	0.66	36.68	46.45	10.22	0.01	0.71	1.04	0.02	-	-	-	96.24
White-mica	0.14	1.22	33.9	48.21	11.05	-	0.01	2.3	0.04	0.07	-	-	96.96
	0.32	1.06	32.94	46.33	9.95	0.03	1.29	4.68	0.06	0.08	-	-	96.74
	0.03	10.27	15.1	35.21	9.29	0.01	3.87	19.83	-	0.5	-	-	94.09
	-	-	0.33	0.05	-	0.01	98.53	0.03	-	-	-	-	98.95
Rutile	-	-	0.67	0.11	-	0.08	94.98	4.19	-	0.06	-	-	100.09
	-	0.02	0.42	0.12	-	0.06	98.3	1.01	-	0.01	-	-	99.94
	-	-	0.31	0.05	-	0.03	100.24	0.05	-	-	-	-	100.68
	-	0.08	0.22	0.03	-	0.01	51.02	48.26	-	1.16	-	-	100.78
	-	0.02	0.25	0.04	-	0.02	52.99	44.52	-	1.99	-	-	99.84
Ilmenite	-	0.04	0.24	0.11	-	0.02	51.63	46.59	-	2.2	-	-	100.82
	-	3.6	0.41	0.04	-	0.03	54.76	40.06	-	0.39	-	-	99.28
	-	2.9	0.36	0.05	-	0.04	46.62	45.92	-	1.63	-	-	97.52
	-	-	n.a.	31.76	-	-	-	-	-	-	65.53	1.36	98.66
	-	-	0.01	31.94	-	0.01	-	-	-	-	65.41	2.1	99.46
Zircon	-	-	0.02	32.43	-	0.01	-	-	-	-	65.81	1.5	99.75
	-	-	0.02	32.23	-	0.01	-	-	-	-	65.27	1.77	99.3
	-	-	0.01	31.31	-	-	-	-	-	-	65.7	1.82	98.85

Table 2. Porosity (vol. %) inferred by means of high-resolution SR micro-CT

Sample/VOI	**Size (mm^3)**	**Pores (vol. %)**
SPR1b Host rock	0.94	17.90
SPR1b comp. band	0.94	6.75
SPR2 Slipped DB	0.91	0.86
SPR2a comp. band	0.91	3.90
SPR4 Host rock	0.94	26.46

Table 3. Porosity values according to Hg porosimetry.

Sample	**Total intruded volume (mm^3/g)**	**Accessible porosity (%)**	**Pore modal dimension (μm)**	**Pore median dimension (μm)**
Host rock	101.68	26.75	25.8×10^{-3}	24.1×10^{-3}
Deformation Band	38.65	15.95	10.3	25.8

S upplementary material (Dataset of DBs scanlines)

Scan Line/Area information

Name	Measure method	Plunge/Dip	Trend/DipDirection	Lentgh (m)	Number of measures
St1 Horiz	Scan Line	0	315	7	58
St1 Vert	Scan Line	78	152	1.65	15
St2	Scan Line	0	116	14	63
St3 Hori.	Scan Line	19	133	14.5	85
St3 Vert.	Scan Line	90	228	2.1	18
St4	Scan Line	141	1	21.6	60
St5	ScanArea	76	215	2.8x2	59
St6	Ad hoc				44
Major	Ad hoc				22

St1

Locality	Inters. (m)	Type	Dip	Dip Direction	Semi-Lentgh (m)	Dislocation		Thickness (mm)
						(cm)	Dx/Sx	
St1 Vert.	1.44	DB	78	112	0.17			1
St1 Vert.	1.4	DB	84	274	0.7			2
St1 Vert.	1.3	DB	69	306	>Hc	18	sx	4
St1 Vert.	1.12	DB	54	287	0.19	1	sx	1
St1 Vert.	1	DB	60	298	0.37			1
St1 Vert.	0.87	DB	24	110	1.4	2	sx	2
St1 Vert.	0.73	DB	38	285	0.46	1	sx	1
St1 Vert.	0.62	DB	31	317	0.6			1
St1 Vert.	0.47	DB	32	158	0.37			1
St1 Vert.	0.44	DB	47	305	0.34	2.5	dx	1
St1 Vert.	0.29	DB	59	311	0.73			2
St1 Vert.	0.24	DB	42	317	0.2			1
St1 Vert.	0.13	DB	49	312	0.11			1
St1 Vert.	0.06	DB	55	326	>Hc			2
St1 Vert.	0.04	DB	53	319	0.63			2

St1 Horiz.	7	DB	66	306	>Hc			4
St1 Horiz.	6.8	DB	71	303	0.53	1	dx	1
St1 Horiz.	6.78	DB	72	314	0.6	1	dx	1
St1 Horiz.	6.68	DB	69	318	0.7			1
St1 Horiz.	6.4	DB	70	316	0.34			1
St1 Horiz.	5.9	DB	48	313	>Hc	3	dx	5
St1 Horiz.	5.73	DB	51	308	1.2	1.5	sx	2
St1 Horiz.	5.56	DB	55	303	0.22			2
St1 Horiz.	5.46	DB	47	357	>Hc	14	sx	3
St1 Horiz.	5	DB	55	356	0.66			2
St1 Horiz.	4.65	DB	59	309	1.58			2
St1 Horiz.	4.51	Bedding	52	203	0.1			
St1 Horiz.	4.28	DB	76	343	0.79	2.5	sx	1
St1 Horiz.	4.21	DB	80	325	1.01	2	sx	1
St1 Horiz.	3.97	DB	78	303	0.43	2	sx	2
St1 Horiz.	3.81	DB	87	334	2.1	5	sx	4
St1 Horiz.	3.79	DB	63	277	>Hc			2
St1 Horiz.	3.56	DB	84	317	0.41			2
St1 Horiz.	3.34	DB	60	312	0.55			1
St1 Horiz.	3.29	DB	42	350	1.28	0.5	sx	2
St1 Horiz.	3	Bedding	76	199	0.3			
St1 Horiz.	2.92	DB	54	338	0.42			2
St1 Horiz.	2.76	Bedding	67	201	0.12			
St1 Horiz.	2.73	DB	84	76	0.17			1
St1 Horiz.	2.7	DB	48	269	0.2			1.5
St1 Horiz.	2.63	DB	56	304	0.34	2.5	dx	2
St1 Horiz.	2.52	DB	64	331	>Hc			5
St1 Horiz.	2.44	DB	61	348	>Hc	4	dx	7
St1 Horiz.	2.41	DB	78	291	0.61			1
St1 Horiz.	2.33	DB	76	307	0.23			1
St1 Horiz.	2.31	DB	75	301	0.34			1
St1 Horiz.	2.29	DB	68	265	1.1			2
St1 Horiz.	2.15	DB	48	333	>Hc			3
St1 Horiz.	1.96	Bedding	65	220	0.16			
St1 Horiz.	1.94	DB	76	261	0.73			2
St1 Horiz.	1.79	Bedding	78	237	0.15			

St1 Horiz.	1.72	DB	89	295	0.65			1
St1 Horiz.	1.67	DB	67	264	0.5			2
St1 Horiz.	1.57	DB	66	293	0.75	2.5	dx	3
St1 Horiz.	1.49	DB	86	94	0.16			1
St1 Horiz.	1.38	DB	86	70	0.27			1
St1 Horiz.	1.32	DB	86	44	0.38			1
St1 Horiz.	1.27	DB	83	66	0.47			1
St1 Horiz.	1.17	DB	53	314	>Hc	14	dx	2
St1 Horiz.	0.97	DB	56	315	0.64			1
St1 Horiz.	0.92	DB	61	233	0.93			1
St1 Horiz.	0.9	DB	73	311	0.36	7	dx	2
St1 Horiz.	0.796	DB	80	320	0.25			2
St1 Horiz.	0.72	DB	72	275	0.31	3.7	sx	1.5
St1 Horiz.	0.62	DB	62	239	0.41			1
St1 Horiz.	0.6	DB	68	262	0.5	5	dx	4
St1 Horiz.	0.56	DB	72	291	0.28	3	dx	2
St1 Horiz.	0.41	DB	51	230	0.35			1
St1 Horiz.	0.3	DB	69	304	0.09	2.5	dx	2
St1 Horiz.	0.18	DB	50	246	0.09			1.5
St1 Horiz.	0.17	DB	81	317	0.05			1.5
St1 Horiz.	0.1	DB	81	326	0.04			1.5
St1 Horiz.	0.06	DB	83	317	0.03			1.5

St2

Locality	**Inters. (m)**	**Type**	**Dip**	**Dip Direction**	**Semi-Lentgh (m)**	**Thickness (mm)**	**Aperture (mm)**
St2	13.5	Joint	63	265	>Hc		20
St2	13	Joint	55	125	0.4		2
St2	12.95	Joint	84	156	0.15		1
St2	12.8	Joint	90	137	0.8		1
St2	12.67	Joint	86	137	1.05		1
St2	12.61	Joint	85	189	0.46		close
St2	12.59	Joint	59	299	0.27		close
St2	12.5	Joint	74	68	0.23		2

St2	12.39	Joint	46	141	0.2		close
St2	12.27	DB	88	125	0.07	3	
St2	12.25	Joint	63	253	1.33		2
St2	12.1	Joint	78	269	0.07		close
St2	11.99	Joint	80	294	0.28		close
St2	11.94	DB	61	229	0.44	1	
St2	11.55	DB	31	108	0.32	2	
St2	11.4	DB	54	282	1.4	5	
St2	11.29	DB	40	273	0.2	2	
St2	11.2	DB	21	131	0.06	1	
St2	11.85	DB	58	265	1.74	2	
St2	11.1	Joint	52	282	1.03		close
St2	10.75	Joint	89	355	0.22		close
St2	10.5	Joint	48	274	0.53		2
St2	10.3	Joint	66	289	1.4		close
St2	9.3	Joint	77	124	0.23		close
St2	9.14	Joint	63	267	0.42		close
St2	9.08	Joint	89	284	0.3		close
St2	9.04	Joint	81	223	0.2		close
St2	8.75	Joint	42	290	1.04		close
St2	8.69	Joint	52	173	0.09		close
St2	8.6	Joint	42	282	>Hc		5
St2	8.4	Joint	46	265	>Hc		3
St2	7.77	Joint	37	281	>Hc		2
St2	7.44	Joint	42	294	5		close
St2	7.16	Joint	79	273	0.36		close
St2	6.98	Joint	69	93	0.28		3
St2	6.85	Joint	89	265	0.15		4
St2	6.65	Joint	57	273	0.5		close
St2	6.45	Joint	56	269	>Hc		5
St2	6.05	Joint	45	277	0.27		close
St2	5.92	Joint	87	337	0.96		1
St2	5.76	Joint	63	46	0.29		1
St2	5.51	Joint	62	244	0.65		5
St2	5.13	Joint	46	268	>Hc		2
St2	5.1	Joint	74	254	1.6		10

St2	4.73	Joint	82	177	0.31	close
St2	4.65	Joint	88	297	0.32	close
St2	4.6	Joint	87	237	1.05	close
St2	4.16	Joint	66	259	0.88	close
St2	3.83	Joint	77	330	0.18	close
St2	3.7	Joint	54	253	>Hc	25
St2	2.85	Joint	81	270	1.12	10
St2	2.5	Joint	82	251	0.77	10
St2	2.23	Joint	82	268	0.55	3
St2	2.17	Joint	66	261	0.15	close
St2	2.13	Joint	84	225	0.18	3
St2	2	Joint	47	299	>Hc	close
St2	1.95	Joint	52	283	1	close
St2	1.75	Joint	71	277	0.7	close
St2	1.08	Joint	56	307	2.5	close
St2	0.93	Joint	78	159	0.12	close
St2	0.8	Joint	48	287	0.26	close
St2	0.5	Joint	89	83	0.16	12
St2	0.4	Joint	81	200	>Hc	400

St3

Locality	Inters. (m)	Type	Dip	Dip Direction	Semi-Lentgh (m)	Disloc. (cm)	Dx/Sx
St3 Vert..	2.1	DB	46	301			
St3 Vert..	1.85	DB	73	162			
St3 Vert..	1.72	DB	7	343			
St3 Vert..	1.66	DB	53	336			
St3 Vert..	1.57	DB	59	268			
St3 Vert..	1.36	DB	23	89			
St3 Vert..	1.45	DB	71	290			
St3 Vert..	1.25	DB	76	183			
St3 Vert..	1.2	DB	40	302			
St3 Vert..	1.01	DB	26	262			
St3 Vert..	1	DB	9	341			
St3 Vert..	0.83	DB	18	236			

St3 Vert..	0.72	DB	67	220			
St3 Vert..	0.68	DB	60	188			
St3 Vert..	0.63	DB	80	192			
St3 Vert..	0.53	DB	47	328			
St3 Vert..	0.4	DB	66	349			
St3 Vert..	0.05	DB	13	49			
St3 Horiz.	14.4	DB	28	33	>Hc		
St3 Horiz.	13.54	DB	33	284	0.48		
St3 Horiz.	13.4	DB	29	313	0.56		
St3 Horiz.	12.8	DB	37	308	0.7		
St3 Horiz.	12.7	DB	46	307	0.66		
St3 Horiz.	12.24	DB	75	274	0.65		
St3 Horiz.	12.06	DB	80	245	0.66		
St3 Horiz.	12.04	DB	78	261	>Hc		
St3 Horiz.	11.45	DB	86	280	0.9		
St3 Horiz.	11.3	DB	15	295	2.32	6	dx
St3 Horiz.	10.88	DB	70	284	1.12		
St3 Horiz.	10.55	DB	8	240	0.37		
St3 Horiz.	10.3	DB	34	3	>Hc	9	dx
St3 Horiz.	10.08	DB	76	280	>Hc		
St3 Horiz.	8.83	DB	60	303	0.84		
St3 Horiz.	8.76	DB	55	306	0.6		
St3 Horiz.	8.1	DB	58	288	2		
St3 Horiz.	8	DB	74	294	0.35		
St3 Horiz.	7.41	DB	49	339	0.83		
St3 Horiz.	7.4	DB	66	28	0.73		
St3 Horiz.	7.35	DB	51	287	0.11		
St3 Horiz.	7.27	DB	79	300	0.15		
St3 Horiz.	6.9	DB	77	9	2.5	4	dx
St3 Horiz.	6.74	DB	59	346	2.05	14	dx
St3 Horiz.	6.24	DB	76	22	>Hc	11	dx
St3 Horiz.	6.18	DB	46	296	0.25		
St3 Horiz.	6.1	DB	49	271	0.3		
St3 Horiz.	6.03	DB	45	300	0.35		
St3 Horiz.	5.86	DB	86	217	1.75		
St3 Horiz.	5.84	DB	44	312	1.52		

St3 Horiz.	5.5	DB	63	303	2.06	4	dx
St3 Horiz.	5.37	DB	36	350	1.15		
St3 Horiz.	5.2	DB	65	31	>Hc		
St3 Horiz.	5.04	DB	48	315	0.12		
St3 Horiz.	4.85	DB	57	321	0.67		
St3 Horiz.	4.74	DB	35	314	0.94		
St3 Horiz.	4.7	DB	56	297	1.41		
St3 Horiz.	4.69	DB	51	11	1.35		
St3 Horiz.	4.4	DB	35	306	1.53		
St3 Horiz.	4.24	DB	57	129	0.3		
St3 Horiz.	4.09	DB	70	27	>Hc		
St3 Horiz.	3.75	DB	70	300	1.58		
St3 Horiz.	3.66	DB	63	355	0.16		
St3 Horiz.	3.55	DB	72	26	0.42		
St3 Horiz.	3.44	DB	52	327	0.3		
St3 Horiz.	3.32	DB	81	336	1.78	1	sx
St3 Horiz.	3.18	DB	76	171	0.3		
St3 Horiz.	3.16	DB	51	325	0.36		
St3 Horiz.	3.05	DB	48	310	0.34		
St3 Horiz.	2.97	DB	68	303	0.3		
St3 Horiz.	2.9	DB	71	303	0.07		
St3 Horiz.	3.08	DB	20	6	0.42		
St3 Horiz.	2.72	DB	22	270	0.2		
St3 Horiz.	2.55	DB	33	286	0.12		
St3 Horiz.	2.58	DB	68	274	0.1		
St3 Horiz.	2.5	DB	73	339	0.08		
St3 Horiz.	2.34	DB	66	28	>Hc		
St3 Horiz.	2.14	DB	32	140	1.1		
St3 Horiz.	2.12	DB	76	170	1.68		
St3 Horiz.	2	DB	42	259	0.15		
St3 Horiz.	1.62	DB	35	143	0.56		
St3 Horiz.	1.82	DB	39	260	0.3		
St3 Horiz.	1.53	DB	28	330	0.43		
St3 Horiz.	1.35	DB	65	302	0.51		
St3 Horiz.	1.1	DB	72	265	0.47		
St3 Horiz.	0.33	DB	6	173	0.9		

St3 Horiz.	0.24	DB	63	306	1.5	1.5	dx
St3 Horiz.	1.35	DB	65	302	0.51		
St3 Horiz.	1.1	DB	72	265	0.47		
St3 Horiz.	0.33	DB	6	173	0.9		
St3 Horiz.	0.24	DB	63	306	1.5	1.5	dx

St4

Locality	**Inters. (m)**	**Type**	**Dip**	**Dip Direction**	**Semi-Length (m)**	**disloc.**	
						(cm)	**dx/sx**
St4	21.6	DB	41	336	>Hc		
St4	21.53	DB	34	316	0.15		
St4	21.45	DB	57	339	0.38		
St4	21.15	DB	60	351	>Hc		
St4	20.78	DB	47	158	0.58		
St4	20.55	DB	66	153	0.8		
St4	20.37	DB	53	145	1.2		
St4	20.29	DB	83	337	1.72		
St4	19.85	DB	60	341	>Hc		
St4	19.34	DB	83	318	0.47		
St4	18.88	DB	55	348	0.92		
St4	18.57	DB	30	72	0.92		
St4	18.54	DB	55	345	0.38		
St4	18.5	DB	75	356	1.23		
St4	18.4	DB	74	336	0.46	2	sx
St4	18.3	DB	53	346	>Hc		
St4	18.1	DB	37	5	0.57		
St4	18	DB	38	64	0.62	2	sx
St4	17.56	DB	60	171	0.76		
St4	17.5	DB	28	91	>Hc	2.5	sx
St4	17.18	DB	44	322	0.73		
St4	16.95	DB	64	168	0.51		
St4	16.87	DB	58	171	0.52		
St4	16.63	DB	29	180	0.35		
St4	15.9	DB	54	212	1.08		
St4	15.8	DB	52	320	0.42		

St4	14.85	DB	34	259	0.67		
St4	14.6	DB	88	162	0.21		
St4	14.51	DB	47	327	0.21		
St4	13.4	DB	63	96	2.22		
St4	12.2	DB	43	92	0.9		
St4	9.25	DB	78	62	>Hc		
St4	8.9	DB	29	93	0.68	1.5	sx
St4	8.53	DB	45	96	1.53	2	sx
St4	8.4	DB	77	3	0.28	2	sx
St4	8.27	DB	75	173	0.62	2.5	sx
St4	6.9	DB	26	183	0.1		
St4	6.8	DB	19	199	0.26		
St4	6.65	DB	36	171	0.19		
St4	6.27	DB	30	184	0.16		
St4	6.2	DB	42	94	0.61		
St4	6.15	DB	33	180	0.14		
St4	6.05	DB	25	181	0.15		
St4	5.75	DB	31	125	2.3	2	sx
St4	4.97	DB	72	171	0.64		
St4	4.55	DB	71	66	>Hc		
St4	3.66	DB	89	231	2.34		
St4	3.2	DB	80	193	0.6		
St4	2.93	DB	46	108	0.29		
St4	2.63	DB	51	352	0.53	3	sx
St4	2.44	DB	60	331	>Hc	34	sx
St4	1.65	DB	72	55	>Hc		
St4	1.3	DB	59	208	0.65		
St4	0.95	DB	52	343	0.61	2	sx
St4	0.7	DB	15	102	0.43	1	sx
St4	0.56	DB	55	358	0.35	3	sx
St4	0.39	DB	68	168	>Hc		
St4	0.3	DB	53	173	0.35	0.5	dx
St4	0.2	DB	68	176	1.63	0.2	dx
St4	0.1	DB	76	351	0.56		
St4	0.3	DB	53	173	0.35	0.5	dx
St4	0.2	DB	68	176	1.63	0.2	dx

St4	0.1	DB	76	351	0.56

St5

Locality	Type	Dip	Dip Direction	Disloc. (cm)	Dx/Sx
St5	DB	41	196		
St5	DB	72	63		
St5	DB	43	186		
St5	DB	41	219		
St5	DB	78	296	1	sx
St5	DB	54	82		
St5	DB	60	189		
St5	DB	51	202		
St5	DB	36	223		
St5	DB	57	332		
St5	DB	72	50		
St5	DB	59	230		
St5	DB	62	93		
St5	DB	51	132		
St5	DB	89	219		
St5	DB	66	72		
St5	DB	78	82		
St5	DB	85	219		
St5	DB	57	275	1.5	dx
St5	DB	59	70		
St5	DB	40	231		
St5	DB	65	268		
St5	DB	48	217		
St5	DB	67	110		
St5	DB	89	220		
St5	DB	46	333		
St5	DB	73	303	3.5	dx
St5	DB	61	349		
St5	DB	62	276		

St5	DB	71	328		
St5	DB	52	220		
St5	DB	87	308		
St5	DB	61	184		
St5	DB	72	272		
St5	DB	61	352		
St5	DB	80	222		
St5	DB	51	267		
St5	DB	67	291		
St5	DB	74	347		
St5	DB	66	277	2	sx
St5	DB	83	298		
St5	DB	60	263		
St5	DB	73	274		
St5	DB	64	338	4	sx
St5	DB	59	285		
St5	DB	60	297		
St5	DB	35	31		
St5	DB	34	338		
St5	DB	40	308		
St5	DB	34	287	0.5	sx
St5	DB	58	281		
St5	DB	55	301		
St5	DB	47	303		
St5	DB	49	318		
St5	DB	67	342		
St5	DB	78	332		
St5	DB	32	283		
St5	DB	50	298	2	dx
St5	DB	50	305		
St5	DB	32	283		
St5	DB	50	298	2	dx
St5	DB	50	305		

St6

Locality	Type	Dip	Dip Direction
St6	Joint	86	192
St6	Joint	60	53
St6	Joint	72	318
St6	Bedding	25	234
St6	Joint	50	54
St6	Joint	11	53
St6	Joint	54	47
St6	Joint	53	59
St6	Joint	60	299
St6	Joint	85	311
St6	Joint	65	59
St6	Joint	89	34
St6	Joint	55	71
St6	Joint	85	354
St6	Joint	56	64
St6	Joint	41	57
St6	Joint	56	26
St6	Bedding	25	232
St6	Bedding	41	243
St6	Bedding	34	214
St6	Bedding	41	227
St6	Bedding	24	212
St6	Bedding	31	223
St6	Bedding	62	220
St6	Bedding	62	219
St6	Bedding	67	225
St6	Bedding	82	207
St6	Bedding	73	193
St6	Bedding	71	205
St6	Bedding	67	215
St6	Bedding	47	222
St6	Bedding	40	215

St6	Bedding	31	230
St6	Joint	80	308
St6	Bedding	54	210
St6	Bedding	56	210
St6	Joint	64	274
St6	Joint	77	296
St6	Joint	61	321
St6	Joint	49	323
St6	Bedding	43	209
St6	Bedding	52	220
St6	Bedding	54	214
St6	Bedding	49	200

Major

Locality	Type	Dip	Dip Direction	Disloc. (cm)	Dx/Sx
Major	DB	59	3		
Major	DB	60	318		
Major	DB	62	280		
Major	DB	78	309		
Major	DB	44	319		
Major	DB	17	0		
Major	DB	77	308		
Major	DB	58	357	dx	4
Major	DB	57	20		
Major	DB	51	4		
Major	DB	43	3		
Major	DB	69	333		
Major	DB	36	225		
Major	DB	83	255		
Major	DB	87	214	sx	7
Major	DB	7	236		
Major	DB	6	270		
Major	DB	22	235		

Major	DB	35	206
Major	DB	42	331
Major	DB	53	348
Major	DB	18	249

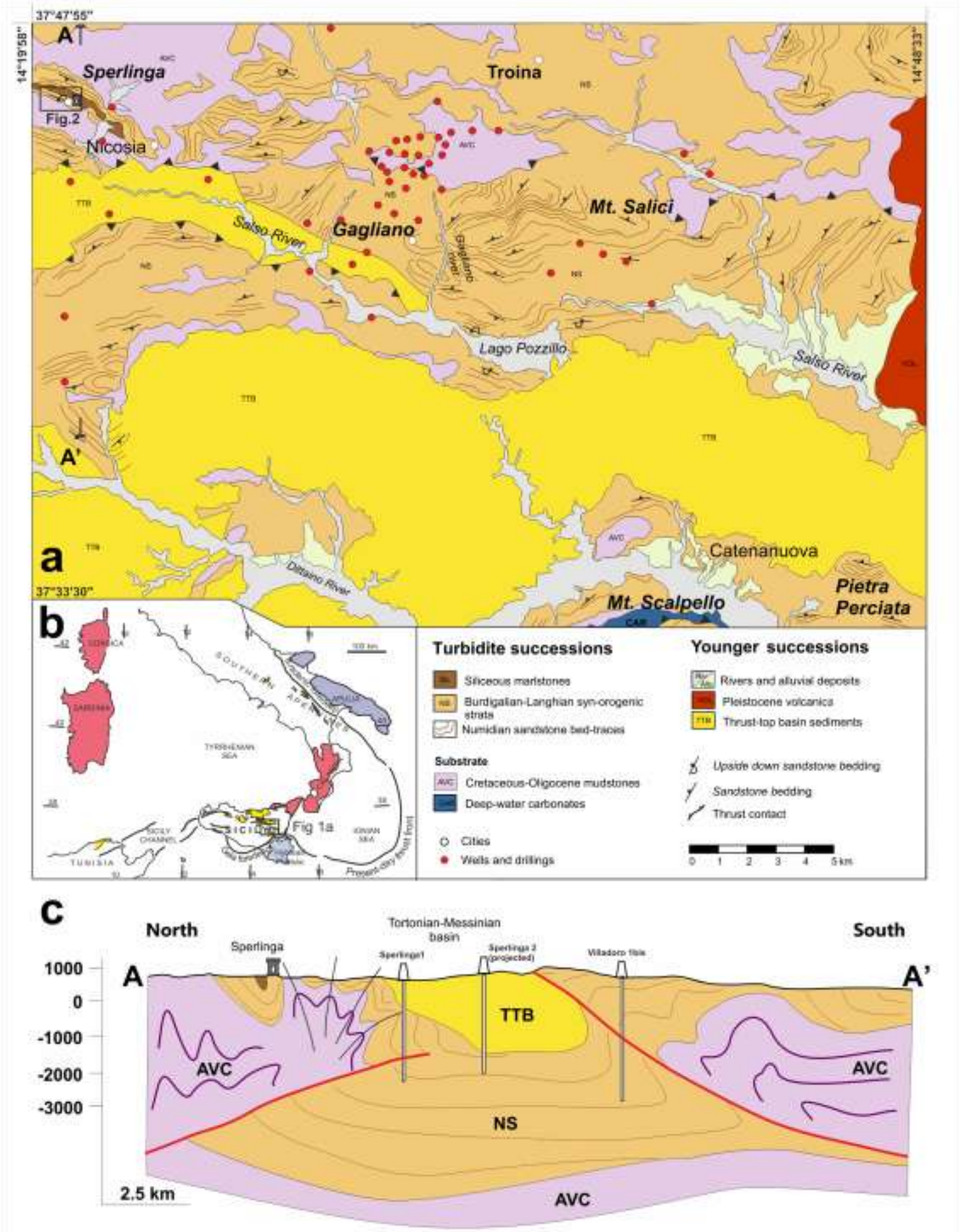

37°47'55''
14°19'58''
14°48'33''
A
Sperlinga
Fig.2
Nicosia
Troina
Gagliano
Mt. Salici
Salso River
Lago Pozzillo
A'
a
37°33'30''
Dittaino River
Catenanuova
Mt. Scalpello
Pietra
Perciata
b
Fig 1a
Turbidite successions
Siliceous marlstones
Burdigalian-Langhian syn-orogenic strata
Numidian sandstone bed-traces
Substrate
Cretaceous-Oligocene mudstones
Deep-water carbonates
Cities
Wells and drillings
Younger successions
Rivers and alluvial deposits
Pleistocene volcanics
Thrust-top basin sediments
Upside down sandstone bedding
Sandstone bedding
Thrust contact
0 1 2 3 4 5 km
c
North
South
Tortonian-Messinian basin
Sperlinga
1000
0
-1000
-2000
-3000
A
A'
TTB
AVC
NS
AVC
AVC
2.5 km

Figure 1

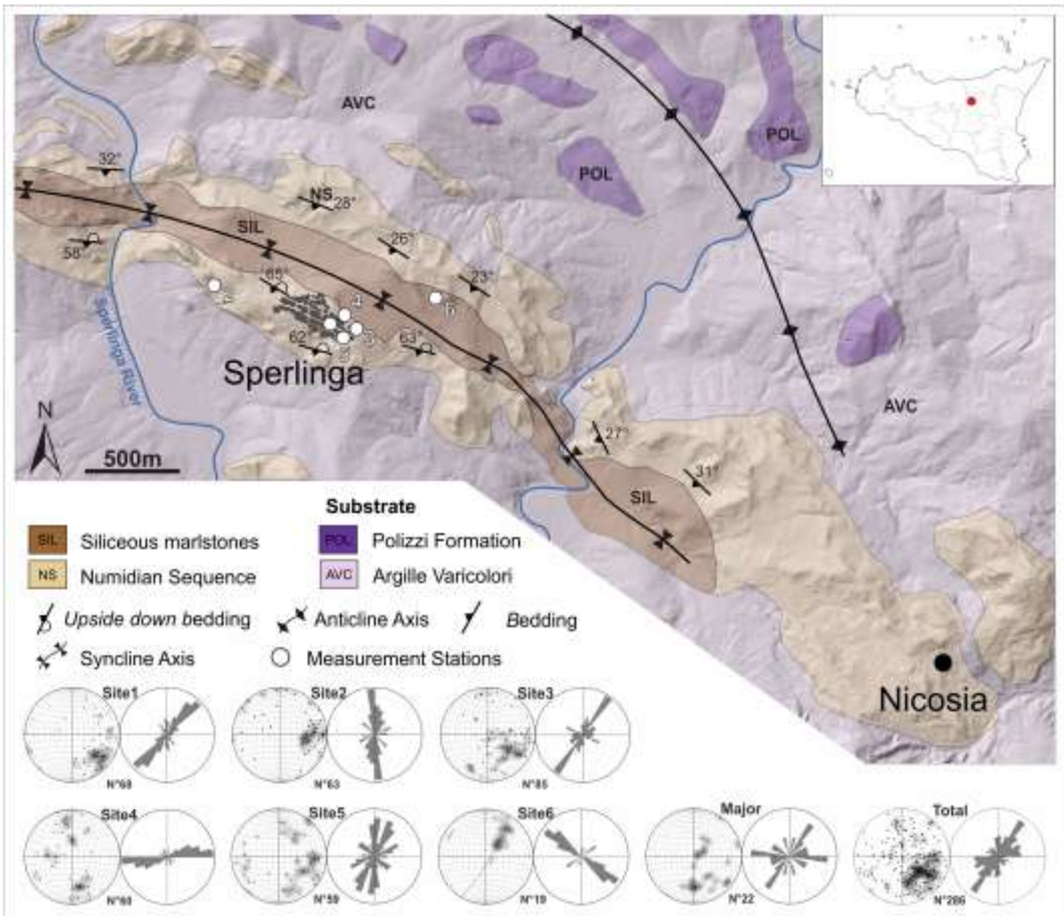

Figure 2

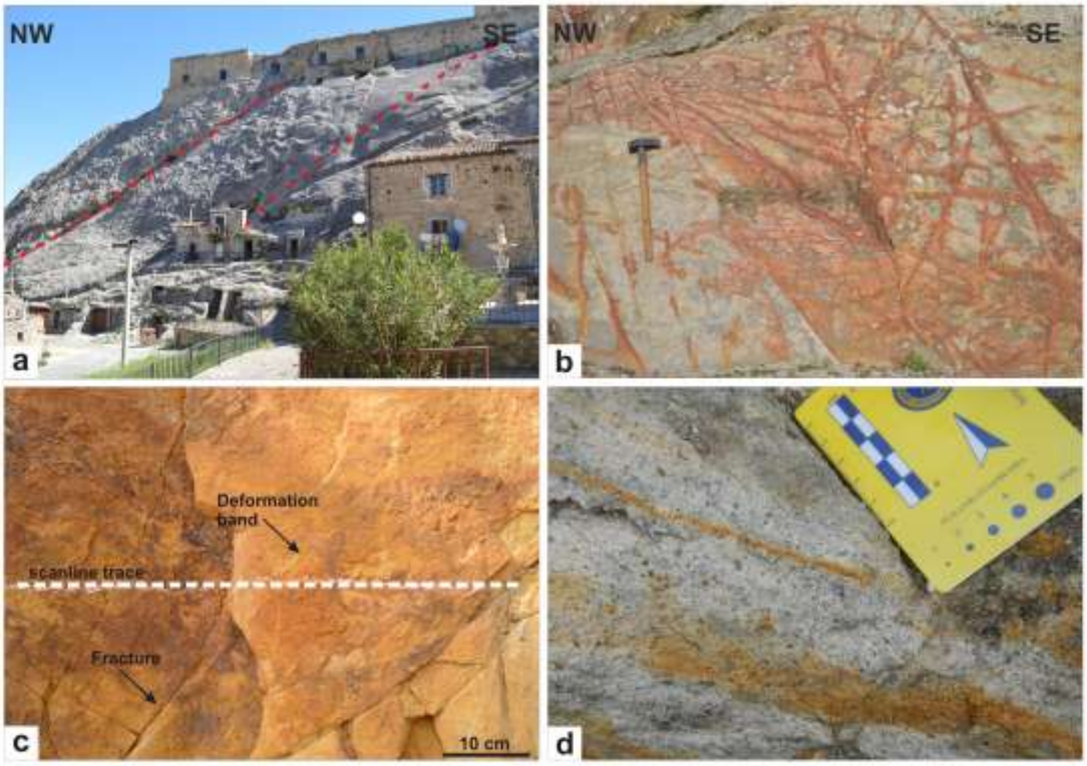

Figure 3

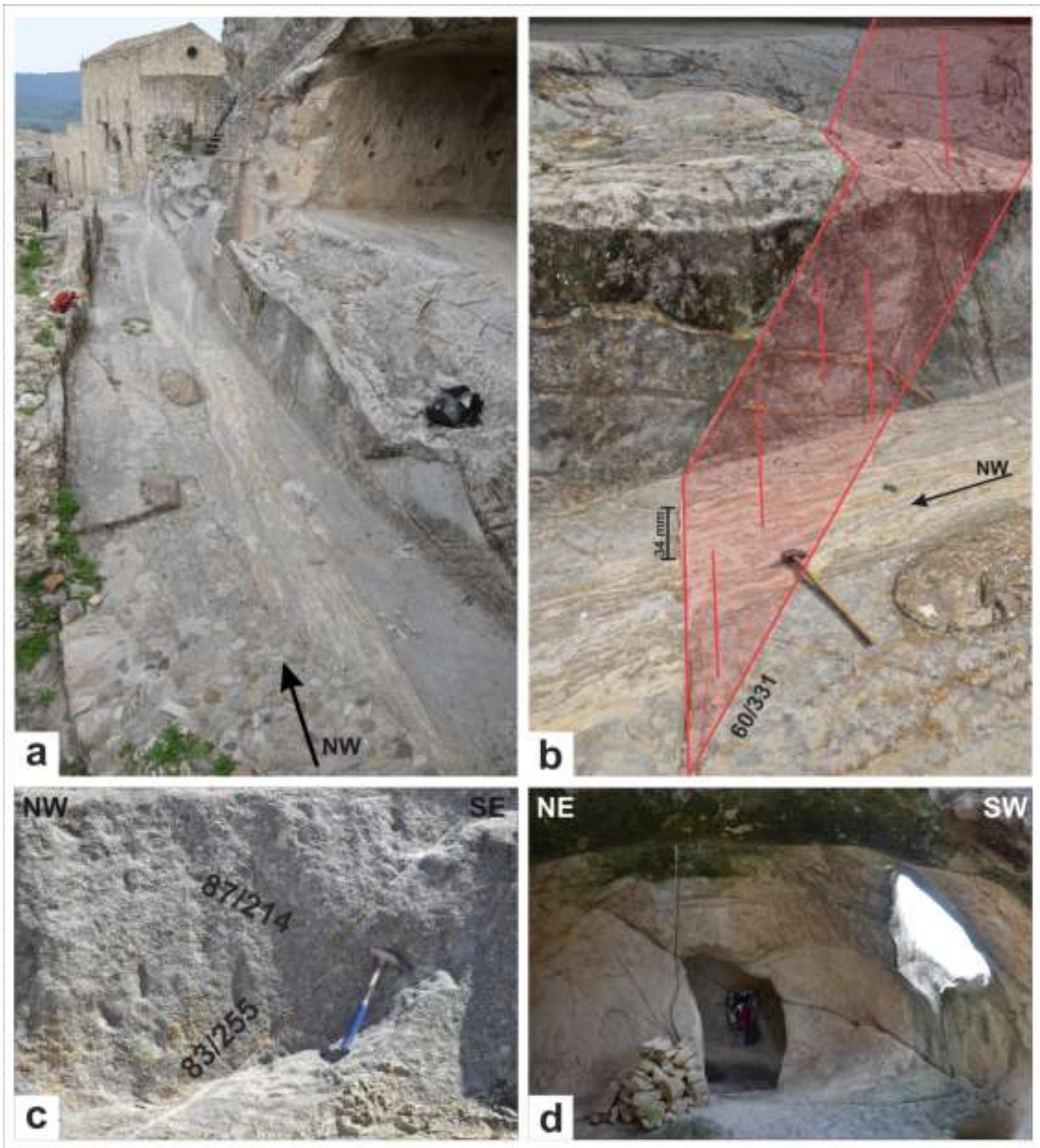

Figure 4

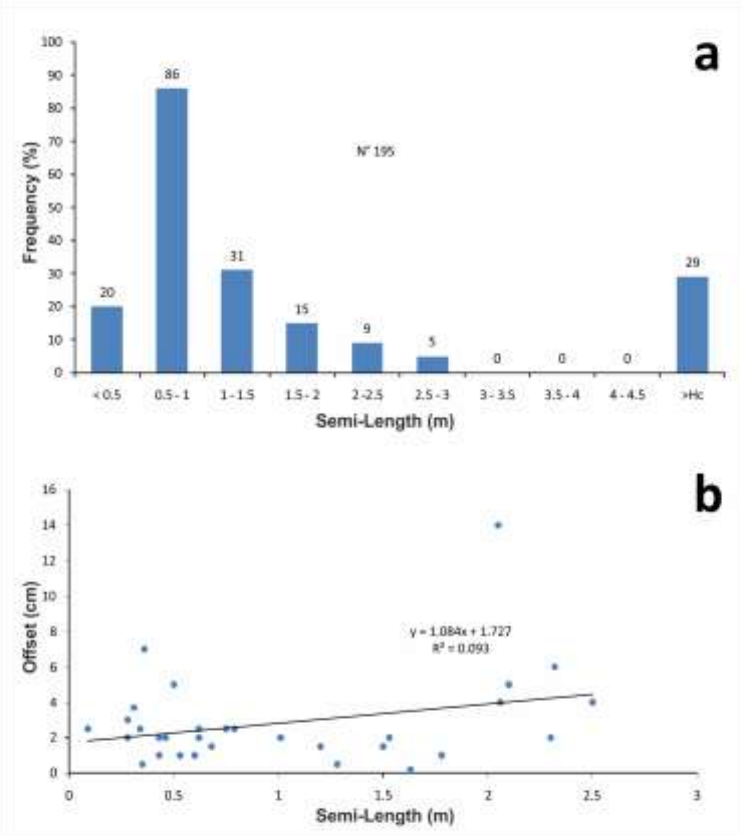
a
Frequency (%)
100
90
80
70
60
50
40
30
20
10
0
86
N° 195
31
29
20
15
9
5
0
0
0
< 0.5
0.5 - 1
1 - 1.5
1.5 - 2
2 -2.5
2.5 - 3
3 - 3.5
3.5 - 4
4 - 4.5
>Hc
Semi-Length (m)
b
Offset (cm)
16
14
12
10
8
6
4
2
0
y = 1.084x + 1.727
R² = 0.093
0
0.5
1
1.5
2
2.5
3
Semi-Length (m)

Figure 5

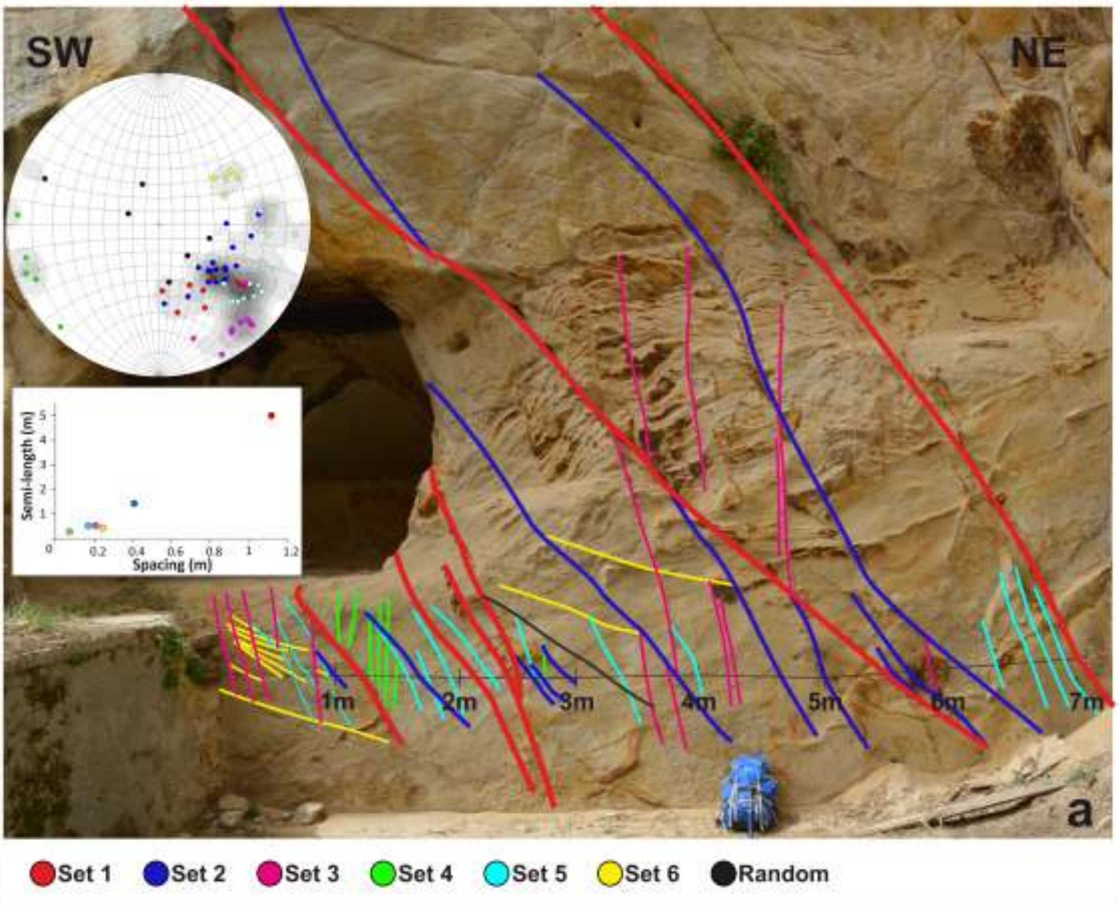

Figure 6

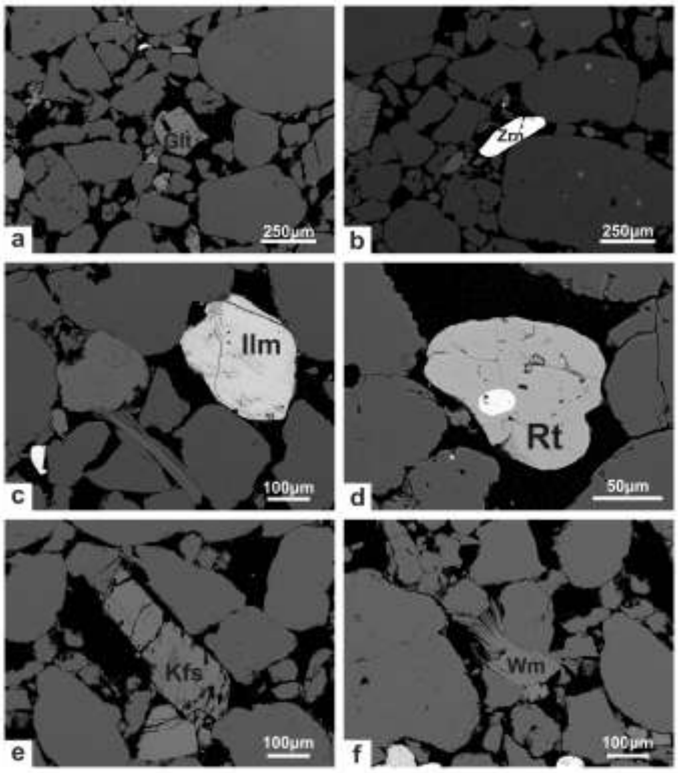

Figure 7

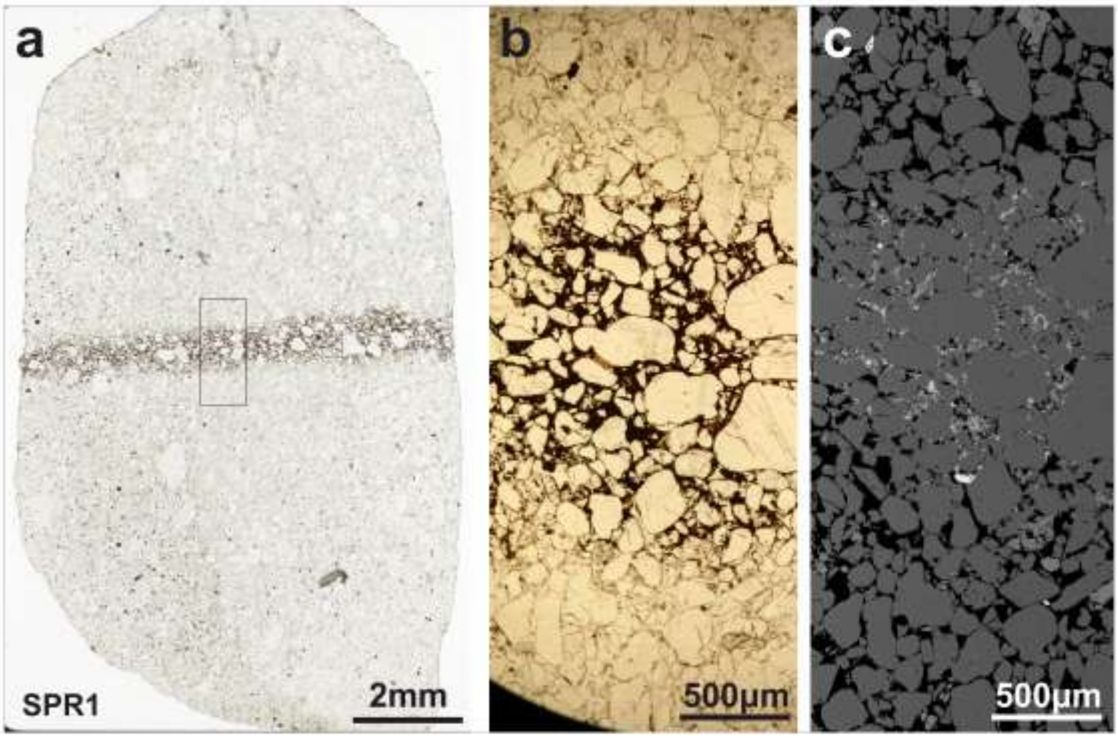

Figure 8

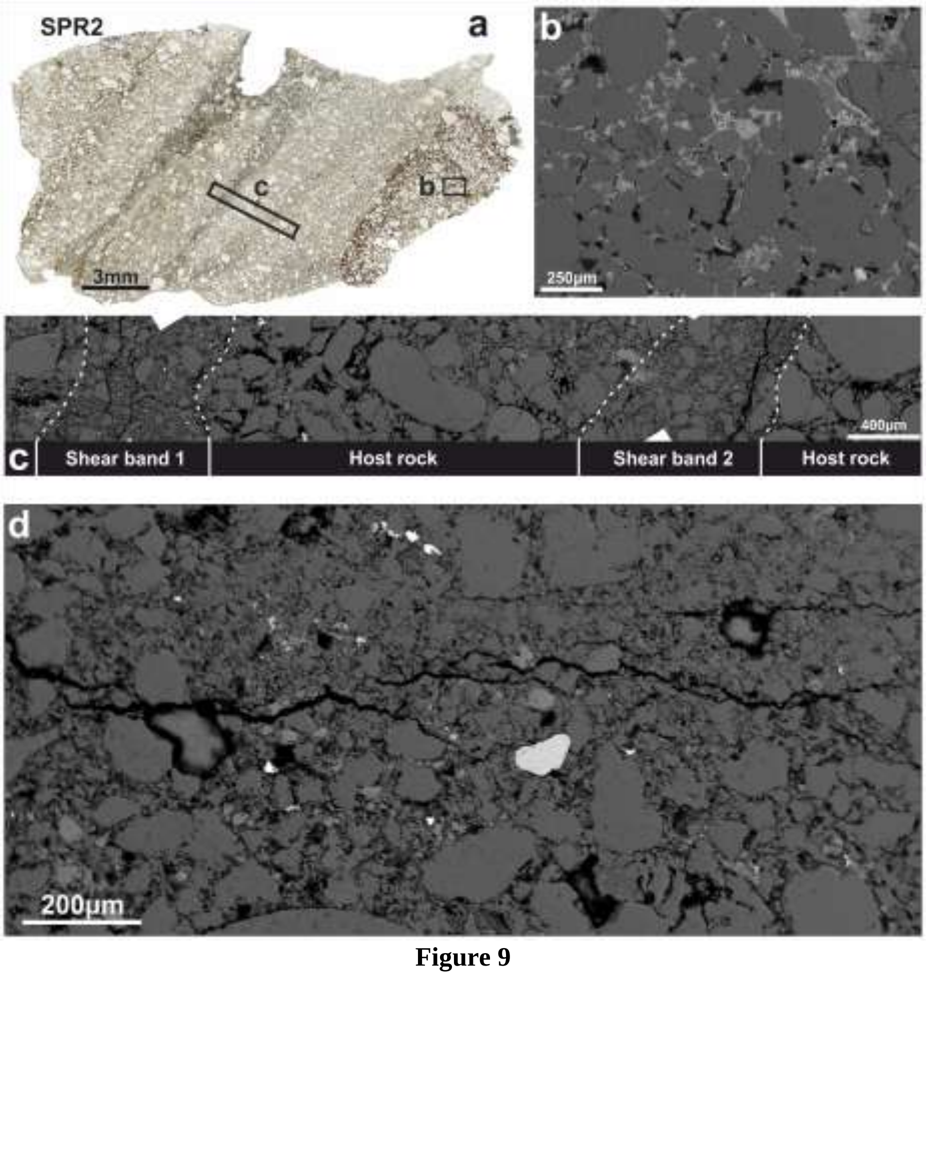

Figure 9

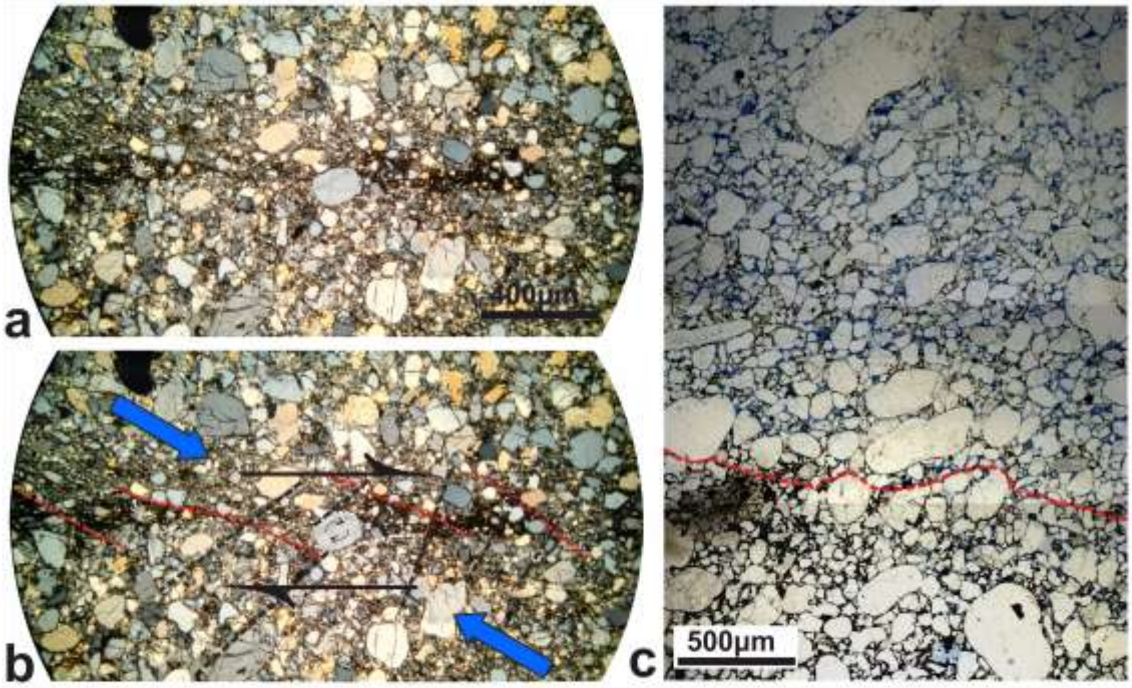

Figure 10

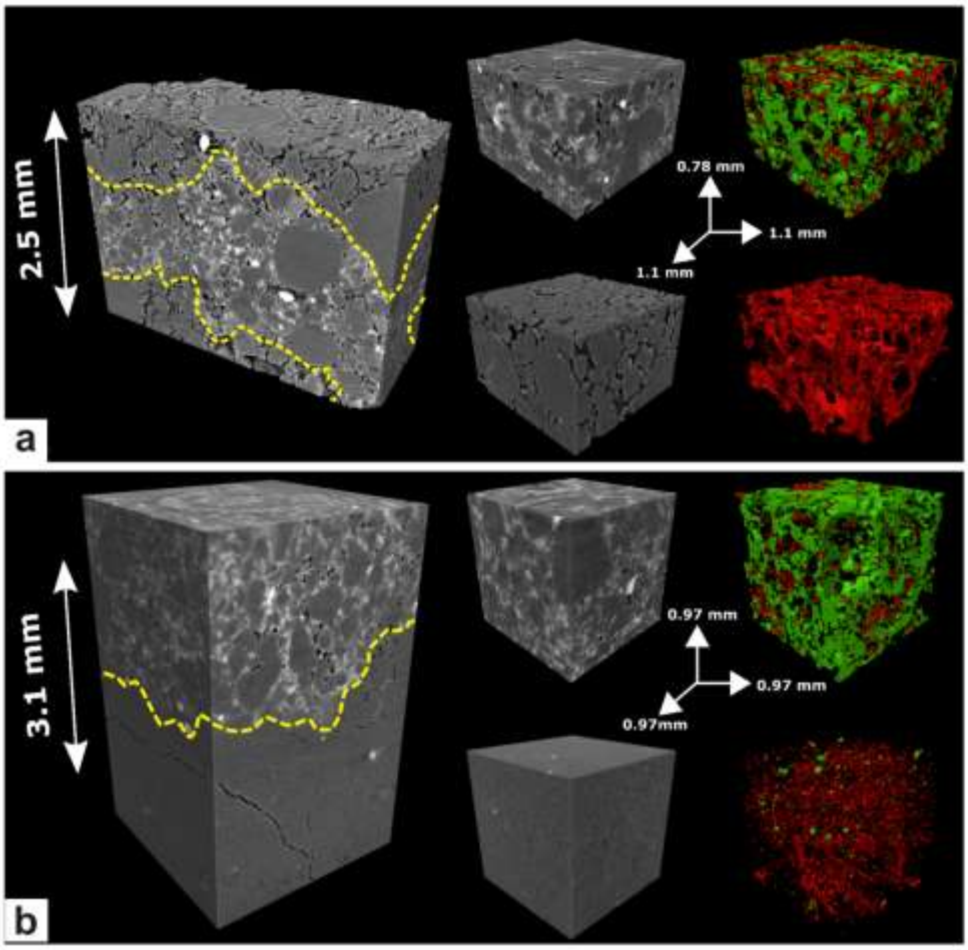

Figure 11

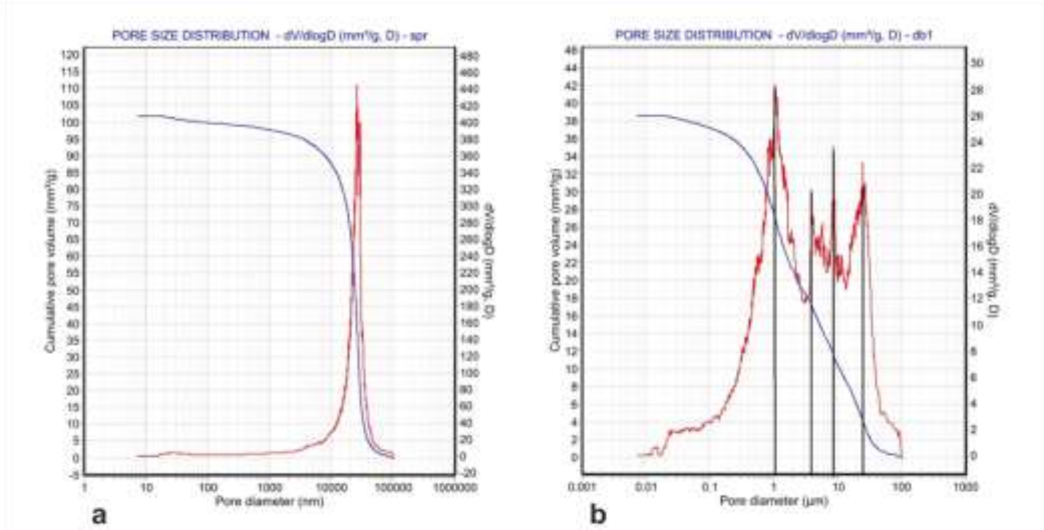

Figure 12

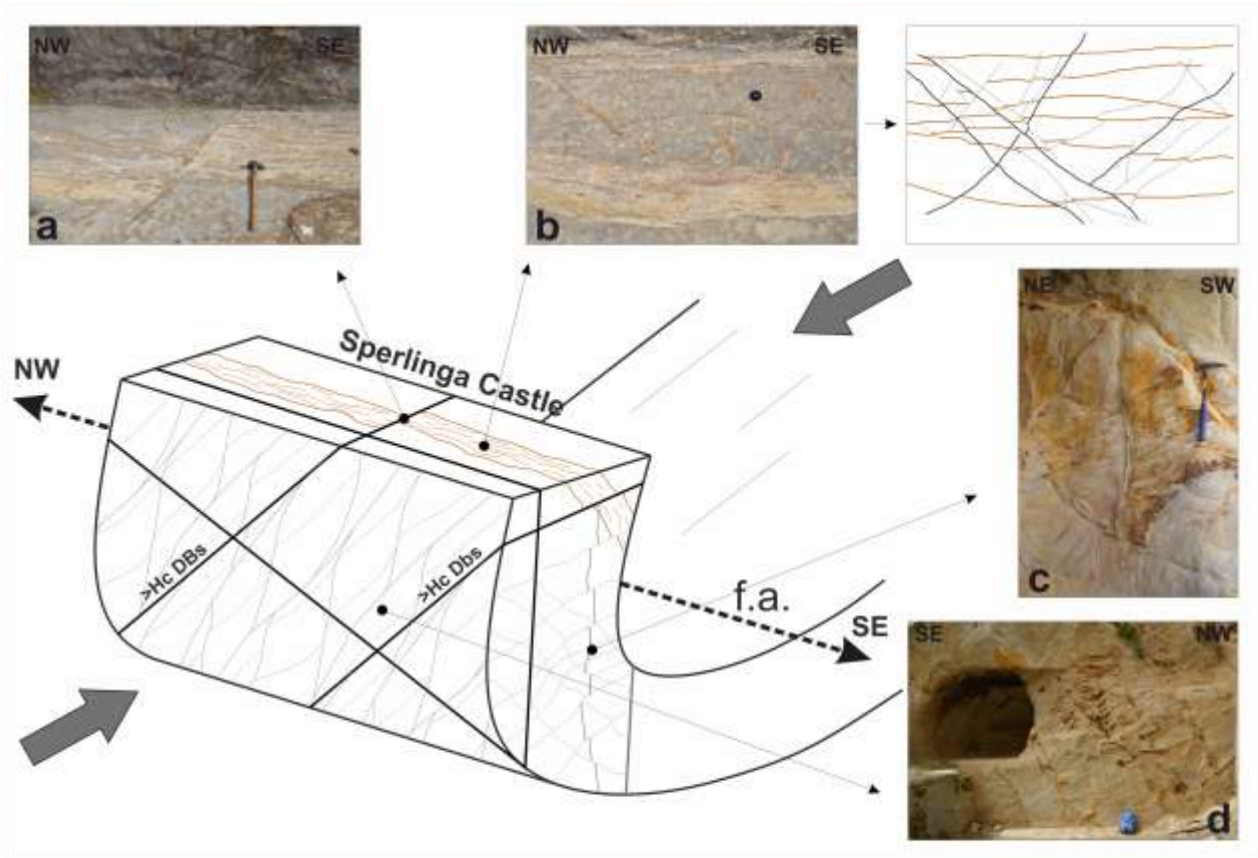

Figure 13

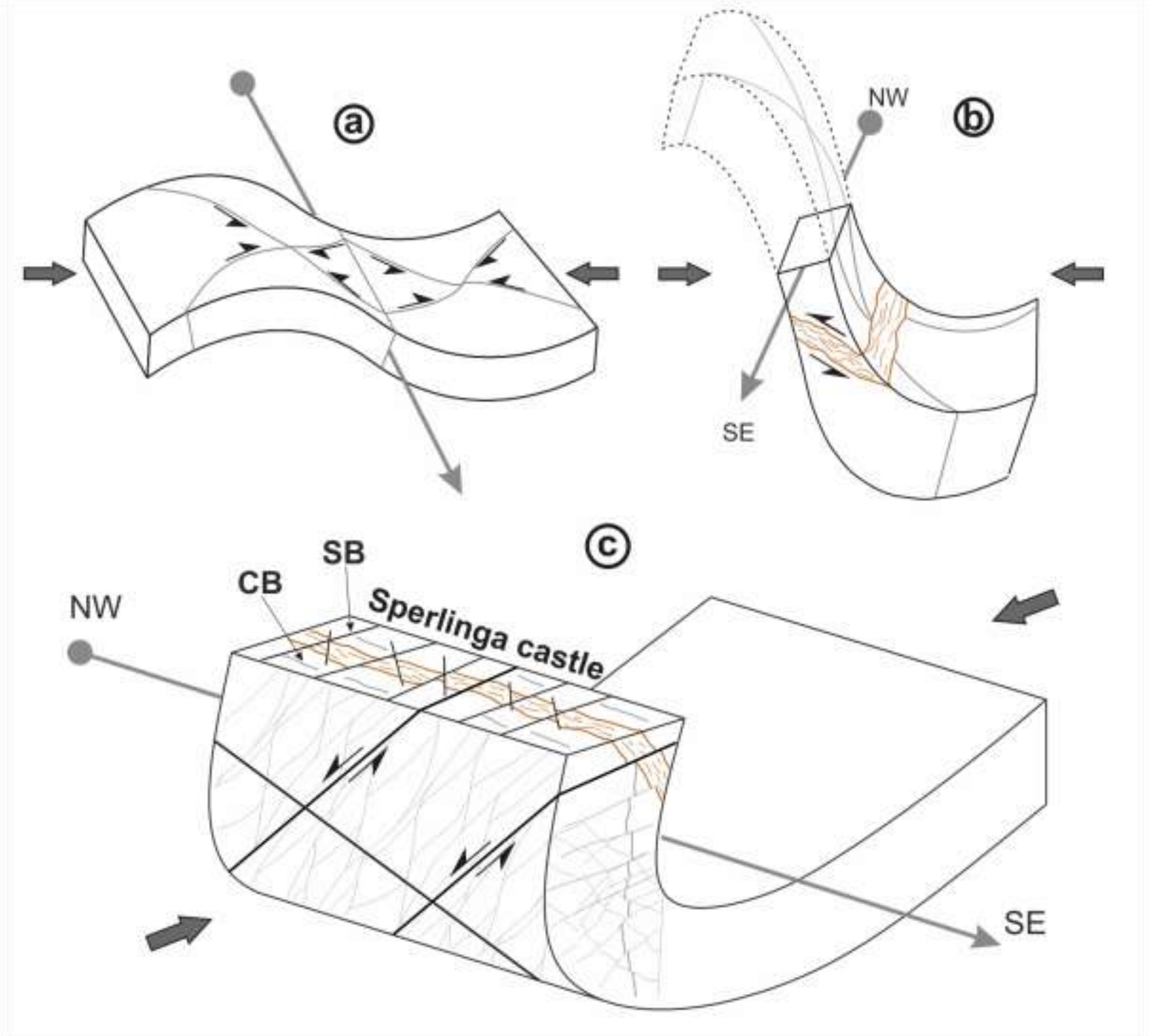

Figure 14